UNIVERSITY OF THESSALY
SCHOOL OF ENGINEERING
DEPARTMENT OF MECHANICAL ENGINEERING

PRELIMINARY CONCEPTUAL DESIGN OF KNUDSEN HEAT PUMP

by
ALEXIOS VATIS

Submitted in partial fulfillment of the requirements for the degree of Diploma in Mechanical Engineering at the University of Thessaly

Volos, 2025

Approved by the Committee on Final Examination:

Advisor	Prof. Dimitris Valougeorgis, Professor, Department of Mechanical Engineering, University of Thessaly
Member	Dr. Giorgos Tatsios, Department of Mechanical Engineering, University of Thessaly
Member	Prof. Vasilis Bontozoglou, Professor, Department of Mechanical Engineering, University of Thessaly

Date Approved: [June 27, 2025]

PRELIMINARY CONCEPTUAL DESIGN OF KNUDSEN HEAT PUMP

Alexios Vatis

Department of Mechanical Engineering, University of Thessaly, 2025

Supervisor: Prof. Dimitris Valougeorgis

Abstract

The so-called Knudsen heat pump (KHP) is a micro heat pump, where the conventional compressor is replaced by a gas micro compressor, also known as the Knudsen compressor, which is operating without moving parts, based on the thermal transpiration (or thermal creep) phenomenon. Recently, several experimental efforts have been performed, worldwide, to construct, test and monitor the performance of Knudsen heat pumps, including a promising one at the University of Nagoya and Toyota Central R&D Labs in Japan, where the Knudsen compressor is a porous glass fiber filter, the evaporator and the condenser are typical micro heat exchangers and the working fluid is water/vapor.

Here, this specific experimental setup is simulated, based on an existing mathematical model and computer code for Knudsen heat pumps, developed at the Laboratory of Physical Processes and Process Equipment at the University of Thessaly. The porous medium is approximated by a circular disk of finite length, with parallel circular capillaries and the mass flow rate is calculated using the linearized Shakhov model. The computational model closely employs the experimental geometric parameters and operating conditions.

In the present work extensive computational results are obtained in a wide range of all involved parameters. The computed quantities include the operating conditions at each heat pump stage, the mass flow rate, the heat flows in the evaporator and the condenser, the coefficient of performance and the overall heat pump efficiency. A detailed comparison with the corresponding experimental results is performed for five different sets of measured temperatures, named Cases I-V. The effect of the geometry data, such as the length, diameter

and tortuosity of the capillaries, as well as of the operating data, such as the evaporator and condenser temperatures, are investigated in detail.

The computational results are, in some cases, in reasonably good agreement with experimental data, while in other cases, significant discrepancies are observed. It has been found that the assumed material porosity and channel tortuosity are of major importance and significantly affect the KHP performance. The evaporator and condenser temperatures are also of major importance. These measured temperatures are very close to each other and therefore, very small temperature variations, even of less than 0.5%, result in significant changes in the temperature difference between the condenser and the evaporator, deducing large changes in the computed mass flow rate and heat flows.

Overall, the effectiveness of the employed model is well demonstrated. Furthermore, via the detailed comparison with the experimental data and the comprehensive parametric analysis, the key geometric and operational parameters affecting the performance of the Knudsen compressor and the Knudsen heat pump have been identified. Further work is needed to relax some of the modeling assumptions and improve measurement accuracy, in order to develop commercial KHP as a promising alternative to conventional micro heat pumps for enhanced energy efficiency and environmental sustainability.

Key words: Knudsen heat pump, Knudsen compressor, kinetic theory, porous material.

ΠΡΟΚΑΤΑΡΚΤΙΚΟΣ ΣΧΕΔΙΑΣΜΟΣ ΑΝΤΛΙΑΣ ΘΕΡΜΟΤΗΤΑΣ ΜΕ ΣΥΜΠΙΕΣΤΗ KNUDSEN

Αλέξιος Βατής
Τμήμα Μηχανολόγων Μηχανικών, Πανεπιστήμιο Θεσσαλίας, 2025

Επιβλέπων Καθηγητής: Δημήτρης Βαλουγεώργης

Περίληψη

Η αποκαλούμενη αντλία θερμότητας Knudsen (KHP) αποτελεί μια μικρο-αντλία θερμότητας, όπου ο συμβατικός μηχανικός συμπιεστής αντικαθίσταται από έναν μικροσυμπιεστή αερίου τύπου Knudsen, ο οποίος λειτουργεί χωρίς κινούμενα μέρη, αξιοποιώντας το φαινόμενο της θερμικής ολίσθησης (thermal transpiration ή thermal creep). Τα τελευταία χρόνια έχουν πραγματοποιηθεί διεθνώς αρκετές πειραματικές προσπάθειες κατασκευής και αξιολόγησης τέτοιων συστημάτων, με ιδιαίτερα ελπιδοφόρα εκείνη του Πανεπιστημίου Nagoya και των Toyota Central R&D Labs στην Ιαπωνία, όπου ο συμπιεστής Knudsen είναι ένα πορώδες υλικό υαλονήματος, οι εναλλάκτες θερμότητας (εξατμιστής και συμπυκνωτής) είναι μικρο-εναλλάκτες και το ρευστό εργασίας είναι νερό/ατμός.

Στην παρούσα εργασία προσομοιώνεται το συγκεκριμένο πειραματικό μοντέλο, βασισμένο σε υφιστάμενο μαθηματικό μοντέλο και υπολογιστικό κώδικα που έχουν αναπτυχθεί στο Εργαστήριο Φυσικών Διεργασιών και Εξοπλισμού Διεργασιών του Πανεπιστημίου Θεσσαλίας. Το πορώδες μέσο προσεγγίζεται ως κυκλικός δίσκος πεπερασμένου μήκους, με παράλληλα κυλινδρικά κανάλια μικρής διατομής, ενώ η παροχή μάζας υπολογίζεται με το γραμμικοποιημένο μοντέλο Shakhov. Το υπολογιστικό σχήμα υιοθετεί πιστά τα γεωμετρικά και λειτουργικά δεδομένα του πειράματος.

Παράγονται εκτεταμένα αριθμητικά αποτελέσματα για ευρύ φάσμα παραμέτρων. Υπολογίζονται οι συνθήκες λειτουργίας σε κάθε βαθμίδα του κύκλου, η παροχή μάζας, οι θερμικές ροές σε εξατμιστή και συμπυκνωτή, ο συντελεστής απόδοσης (COP) και η συνολική ενεργειακή απόδοση της KHP. Πραγματοποιείται λεπτομερής σύγκριση με τα αντίστοιχα πειραματικά δεδομένα για πέντε διαφορετικές σειρές μετρούμενων θερμοκρασιών (Περιπτώσεις I–V). Διερευνάται αναλυτικά η επίδραση γεωμετρικών παραμέτρων—μήκος, διάμετρος και στρέβλωση (tortuosity) των καναλιών—καθώς και λειτουργικών παραμέτρων, όπως οι θερμοκρασίες εξατμιστή και συμπυκνωτή.

Τα υπολογιστικά αποτελέσματα συμφωνούν ικανοποιητικά με τα πειραματικά σε ορισμένες περιπτώσεις, ενώ σε άλλες εμφανίζονται σημαντικές αποκλίσεις. Διαπιστώθηκε ότι το πόσο πορώδες είναι το υλικό και η στρέβλωση των καναλιών επηρεάζουν καθοριστικά την απόδοση της ΚΗΡ. Εξίσου κρίσιμες είναι οι θερμοκρασίες εξατμιστή και συμπυκνωτή, οι οποίες απέχουν ελάχιστα μεταξύ τους και ως επακόλουθο ακόμη και μεταβολές μικρότερες του 0,5% επιφέρουν σημαντικές αλλαγές στη διαφορά θερμοκρασίας και, κατ' επέκταση, μεγάλες διαφοροποιήσεις στην υπολογιζόμενη παροχή μάζας και στις θερμικές ροές.

Συνολικά, η αποτελεσματικότητα του μοντέλου επιβεβαιώνεται, ενώ από τη σύγκριση με τα πειραματικά δεδομένα και την παραμετρική ανάλυση αναδεικνύονται οι βασικές γεωμετρικές και λειτουργικές παράμετροι που καθορίζουν την απόδοση του συμπιεστή Knudsen και της αντλίας θερμότητας. Απαιτείται περαιτέρω έλεγχος για τη χαλάρωση ορισμένων παραδοχών του μοντέλου και τη βελτίωση της πειραματικής μέτρησης, ώστε να καταστεί δυνατή η ανάπτυξη εμπορικών ΚΗΡ ως πολλά υποσχόμενης εναλλακτικής λύσης έναντι των συμβατικών μικρο-αντλιών θερμότητας, με στόχο την υψηλότερη ενεργειακή απόδοση και τη βιωσιμότητα.

Λέξεις-κλειδιά: αντλία θερμότητας Knudsen, συμπιεστής Knudsen, πορώδες υλικό, κινητική θεωρία

Contents

LIST OF TABLES

LIST OF FIGURES

Chapter 1 **INTRODUCTION**

This chapter presents the basics of kinetic theory and its historical development, tracing key contributions by Maxwell and Boltzmann. It explores the transition from continuum to rarefied gas behavior, highlighting the limitations of the Boltzmann equation. Practical computational approaches, like Shakhov kinetic model, are then surveyed. Their respective advantages and challenges underscore the complexity of modeling rarefied flows.

1.1 Knudsen number and flow regimes

When a gas is in or near equilibrium—meaning that properties such as pressure, temperature, and velocity are well-defined and vary smoothly over characteristic lengths much larger than the molecular free path—it can be treated as a continuous medium. This macroscopic scale enables the use of continuum mechanics and thermodynamics to model transport phenomena such as heat conduction and fluid flow. Modeling is based on macroscopic equations, such as the Navier–Stokes equations derived from the conservation laws of mass, momentum, and energy, where closure is provided by the constitutive laws of Newton, Fourier, and Fick, incorporating transport coefficients (dynamic viscosity μ, thermal conductivity k, and diffusivity D) to account for molecular interactions at a macroscopic level. The continuum-based approach is widely applicable in engineering and scientific problems, where the characteristic dimensions are large compared to the mean free path, ensuring the validity of continuum assumptions.

However, as systems become more rarefied, i.e. quantities change substantially in scales of the order of the mean free path, these assumptions begin to break down, and accurate modeling requires alternative, more fundamental, approaches. One such approach is kinetic theory, a branch of statistical mechanics that describes the behavior of gases by analyzing the motion and interactions of molecules [1]. By employing a statistical approach, typically through a molecular velocity distribution function, kinetic theory bridges the microscopic and macroscopic scales, offering insights into phenomena such as viscosity, thermal conductivity, and diffusion. Its importance lies in its ability to model gas dynamics across a wide range of

conditions, including both equilibrium and far-from-equilibrium states, making it essential for understanding and predicting transport phenomena in dilute gases. Kinetic theory finds extensive applications in fields such as high-altitude aerodynamics [2,3], porous media (e.g., membranes and filters) [4], and Microelectromechanical Systems (MEMS) [5,6].

To determine whether a gas should be treated as a continuum or as rarefied, a dimensionless number called the Knudsen number (*Kn*) is introduced [7]. The Knudsen number compares the mean free path λ of gas molecules to a characteristic length scale L_C (e.g., the diameter of a tube):

$$Kn = \frac{\lambda}{L_c} \approx \frac{1}{\delta} \tag{1.1}$$

where δ is sometimes referred to as the "rarefaction parameter", defined as the inverse of *Kn*. When *Kn* is small (or δ is large), the gas behaves like a continuum. As *Kn* increases, the flow transitions to more rarefied states. Conventionally, four distinct rarefaction regimes are identified [8]:

1. Hydrodynamic (Continuum) Regime ($Kn < 10^{-2}$ *or* $\delta > 10^2$): The mean free path is much smaller than the characteristic length ($\lambda \ll L_c$), and molecular interactions are frequent. In this regime, the continuum mechanics equations (e.g., Navier–Stokes) remain valid.
2. Slip Flow Regime ($10^{-2} < Kn < 10^{-1}$ *or* $10 < \delta < 10^2$): In this regime, the conventional no-slip velocity and temperature continuity boundary conditions on surfaces no longer hold, and must be replaced with velocity-slip and temperature-jump conditions. Nevertheless, the bulk flow can still be described by continuum-based equations with modified boundary conditions.
3. Transition Regime ($10^{-1} < Kn < 10$ *or* $10^{-1} < \delta < 10$): Here, the continuum equations break down, and a more fundamental approach, typically via the Boltzmann equation (BE) or other kinetic models, is necessary.
4. Free Molecular (Collisionless) Regime ($Kn > 10$ *or* $\delta < 10^{-1}$): The mean free path is much larger than the characteristic length ($\lambda \gg L_C$), so molecular collisions are rare. Gas molecules predominantly interact with surfaces, rendering intermolecular collisions negligible.

1.2 Kinetic theory basics

Kinetic theory has played a pivotal role in the development of modern gas dynamics, statistical mechanics, and thermodynamics. One major breakthrough came when Maxwell introduced a statistical framework for describing gas behavior. He proposed that gas molecules move independently, each having a range of possible velocities rather than a single uniform speed. This insight led to the derivation of the Maxwell velocity distribution function, Equation (1.2), which describes the probability density of molecular velocities in a gas at thermal equilibrium. Importantly, Maxwell's distribution illustrates that macroscopic properties—such as temperature and pressure—emerge from the collective, statistical behavior of individual molecules [9]:

$$f^M = \frac{N}{(2\pi RT)^{\frac{3}{2}}} \exp\left[-\frac{\left(\tilde{\boldsymbol{\xi}} - \tilde{\boldsymbol{u}}\right)^2}{2RT}\right] \tag{1.2}$$

where $\tilde{\boldsymbol{\xi}}$ is the molecular velocity, $\tilde{\boldsymbol{u}}$ the hydrodynamic velocity, N the number density (number of particles per cubic meter), R the specific gas constant and T the temperature.

Building on Maxwell's theory, Boltzmann advanced the field by formulating an equation describing the temporal and spatial evolution of the velocity distribution function (VDF). Known as the Boltzmann Equation (BE), this integro-differential equation accounts for molecular collisions and their influence on the VDF. Boltzmann showed that the Maxwellian velocity distribution naturally emerges as the equilibrium solution of this equation, reinforcing the statistical nature of gas dynamics. The BE relies on two main assumptions [10]:

1. Binary molecular collisions, limiting its applicability to relatively dilute gases, and
2. Molecular chaos (Stosszahlansatz), which assumes that the velocities of colliding molecules are uncorrelated prior to interaction.

This latter assumption ensures the equation predicts an irreversible approach to equilibrium, despite the time-reversible nature of the underlying microscopic equations of motion. The Boltzmann Equation is commonly written as:

$$\left(\frac{\partial}{\partial t} + \tilde{\boldsymbol{\xi}}_{\mathbf{1}} \cdot \nabla_r + \tilde{\boldsymbol{F}} \cdot \nabla_{\xi_1}\right) f_1 = \iiint (f_1' f_2' - f_1 f_2) g b db d\varphi d\tilde{\boldsymbol{\xi}}_{\mathbf{2}} \tag{1.3}$$

where $\tilde{\boldsymbol{\xi}}_{\mathbf{1}}, \tilde{\boldsymbol{\xi}}_{\mathbf{2}}$ are the molecular velocities before the collision, ∇_r, ∇_{ξ_1} are the gradient operators with respect to r , ξ_1, $\tilde{\boldsymbol{F}}$ is the external force per unit mass applied on the molecules, f_1, f_2 and $f_1' f_2'$ are distribution functions before and after collision respectively, $g = \left|\tilde{\boldsymbol{\xi}}_{\mathbf{2}} - \tilde{\boldsymbol{\xi}}_{\mathbf{1}}\right|$ is the relative velocity before the collision, b is the impact parameter, i.e. the

distance between the asymptotes of a molecule at rest and another at a trajectory and φ is the azimuthal angle specifying the collision geometry.

Among Boltzmann's most significant contributions is the derivation of the H-theorem, which provides a statistical basis for the second law of thermodynamics. The H-theorem states that the quantity

$$H_M = \int f ln(f)\, d\boldsymbol{\xi} \tag{1.4}$$

monotonically decreases over time unless the system is already in equilibrium. In physical terms, it indicates that molecular collisions drive a gas toward a state of maximum entropy. By demonstrating entropy growth in an isolated system, the H-theorem bridges microscopic kinetic theory with macroscopic thermodynamics. Initially called the E-theorem (for "entropy") by Boltzmann, it is now recognized as a microscopic explanation of the second law of thermodynamics. The connection between the H-function and entropy is commonly expressed as

$$S = -k_B H_M + c \tag{1.5}$$

where S is the entropy, H_M the H-function, k_B the Boltzmann's constant and c a constant reflecting the arbitrariness of the zero point of entropy.

1.3 Kinetic Models

The Boltzmann equation constitutes a fundamental framework in rarefied gas dynamics and kinetic theory, offering a statistical description of gas behavior derived from first principles. Its formulation enables the capture of essential non-equilibrium phenomena such as velocity slip, thermal creep, and the development of Knudsen layers. Moreover, the Boltzmann equation inherently incorporates key transport phenomena, including viscosity, thermal conductivity, and diffusion, by correctly modeling molecular interactions via its collision integral.

Despite its theoretical comprehensiveness, the practical application of the Boltzmann equation is considerably hindered by its computational complexity. The equation is an integro-differential equation defined in a seven-dimensional space—comprising three spatial dimensions, three molecular velocity dimensions, and time—which renders its numerical solution particularly challenging. The intricate evaluation of the collision integral, a term that encapsulates the effects of intermolecular collisions, further compounds the computational burden. This integral, typically expressed as

$$Q(f,f) = \iiint (f_1' f_2' - f_1 f_2) g b db d\varphi d\tilde{\boldsymbol{\xi}}_2 \tag{1.6}$$

must satisfy fundamental properties to ensure physical consistency [10]. Among these, the conservation of mass, momentum, and energy (the collision invariants)

$$\int \psi(\boldsymbol{\xi}) J(f) d\tilde{\boldsymbol{\xi}} = 0 \tag{1.7}$$

where $\psi(\boldsymbol{\xi}) = 1, m\tilde{\boldsymbol{\xi}}, m\frac{\boldsymbol{\xi}^2}{2}$, the validity of the H-theorem (which guarantees entropy production and the eventual approach to equilibrium)

$$\int lnf J(f)\, d\tilde{\boldsymbol{\xi}} \leq 0 \tag{1.8}$$

and the adherence to Galilean invariance are paramount. These constraints pose significant challenges when devising approximations or alternative formulations to the full Boltzmann collision term.

To mitigate these challenges, several alternative kinetic models have been developed. One prominent approach is the Direct Simulation Monte Carlo (DSMC) method, which replaces the deterministic evaluation of the collision integral with a stochastic simulation of molecular collisions. DSMC is especially effective in simulating high-speed and highly rarefied flows. However, the method introduces statistical noise and may become computationally inefficient at low Knudsen numbers due to the large number of particles required for accurate results.

In contrast, deterministic approaches employing kinetic model equations simplify the collision term while retaining the essential physics. A widely used example is the Bhatnagar-Gross-Krook (BGK) model, which approximates the collision term by assuming that the distribution function *f* relaxes toward a local Maxwellian equilibrium distribution f^M at a rate determined by a characteristic collision frequency *v*. The BGK model is formulated as [11]:

$$J_{BGK}(f) = v(f^M - f) \tag{1.9}$$

While the BGK model preserves the conservation laws and satisfies the H-theorem, its simplistic relaxation approach fails to yield the correct Prandtl number, thereby limiting its accuracy in predicting heat transfer. An improvement upon the BGK model is offered by the Shakhov model, which introduces a correction to the equilibrium distribution in order to adjust the heat flux and achieve a more accurate representation of the transport coefficients. The Shakhov equation is expressed as [12]

$$J_S(f) = \frac{P}{\mu}(f^S - f) \tag{1.10}$$

where P is the pressure and f^S equals to

$$f^S = f^M\left(1 + 2\frac{(1-Pr)}{5}\frac{m}{N(k_BT)^2}\tilde{\boldsymbol{Q}}\cdot(\tilde{\boldsymbol{\xi}}-\tilde{\boldsymbol{u}})\left(\frac{(\tilde{\boldsymbol{\xi}}-\tilde{\boldsymbol{u}})^2}{2RT}-\frac{5}{2}\right)\right) \tag{1.11}$$

Here, Pr denotes the Prandtl number, $\tilde{\boldsymbol{Q}}$ is the heat flux vector and f^M is the local Maxwellian distribution. This modification enables the Shakhov model to provide correct expressions for both viscosity and thermal conductivity, thereby improving predictions in regimes where heat transfer is significant. Although the Shakhov model preserves the collision invariants, its full form does not rigorously satisfy the H-theorem; however, its linearized version does adhere to this critical property.

1.4 Thermal creep and Knudsen pump

At rarefied conditions where the mean free path of molecules is comparable to or larger than the characteristic channel dimension, there are several mechanisms that can cause a mass flow rate through the channel connecting two chambers. In the context of the present thesis, two mechanisms are relevant. The first one is called Poiseuille flow and occurs when a pressure gradient exists between the edges of a channel. Similar to continuum regime the fluid flows from the high pressure side to the low pressure. The second mechanism is more intriguing. It is called thermal creep, also known as thermal transpiration, and evokes when there is a temperature gradient along the channel wall. Gas molecules on the hot wall of the channel acquire greater kinetic energy and, upon colliding with the surface, impart a net momentum that drives flow from the cold toward the hot side. Then, the pressure in the hot chamber increases and an inverse Poiseuille type flow is developed. Overall, a net flow from the cold low pressure chamber towards the hot high pressure chamber is created. By exploiting the developed net flow a device can be constructed, which can transfer a gas at rarefied conditions from a low temperature and pressure chamber to a high temperature and pressure chamber, similar to a compressor. This kind of device is called Knudsen Compressor or Knudsen Pump [13-19]. Its fabrication requires an array of very narrow channels, usually achieved by employing a porous medium, and its operation a constant applied temperature gradient to drive the flow.

1.5 Thesis objective and structure

The purpose of this thesis is to explore the possibility of utilizing a Knudsen compressor in the compression stage of a heat pump based on the typical vapor compression refrigeration cycle, and to elaborate on an existing model simulating a Knudsen heat pump [20]. A porous material is utilized as the Knudsen compressor. A reasonable accommodation is made where the porous material is modeled as many parallel channels, where the diameter of each channel is much smaller than the length. As a consequence the gas flowing through the channels is considered rarefied. To simulate the flow through the channels, where both a pressure and temperature gradient is present between the edges, the linearized Shakhov kinetic modeled is applied. Then, comparisons are performed between the numerical and experimental results such as the mass flow through the compressor or the heat flows at the heat exchangers.

The structure of the thesis is as follows: In Chapter 2, a description of the Knudsen heat pump operation is given along with the flow configurations that are used for extracting the mass flow through the Knudsen compressor. Also, the experimental setup, which has been used from the literature to perform the comparisons is described. Next, in Chapter 3, the results of the model are presented and compared to the measured values. Also, a parametric analysis of the Knudsen heat pump and how the geometrical characteristics of the compressor and operating conditions affect the efficiency of the heat pump. Finally, in Chapter 4, a brief summary with the main concluding remarks are stated.

Chapter 2 **BASICS ON HEAT PUMPS, KNUDSEN COMPRESSOR AND RAREFIED PRESSURE AND TEMPERATURE DRIVEN FLOWS**

A description of a common heat pump is provided and how a Knudsen compressor is designed by exploiting a porous material. Then, the flow configuration that is assumed through the porous material is presented, along with the governing kinetic equations and the extraction of the overall dimensionless quantities. Finally, for completeness purposes a short description of the cited experimental flow setup is given.

2.1 Typical heat pump description

Heat pumps are widely used in residential, commercial, and industrial settings because of their energy efficiency and versatility. In homes, they provide space heating, cooling, and water heating, ensuring year-round comfort while minimizing energy consumption. Commercial applications include HVAC systems for offices, retail stores, and hotels, where heat pumps deliver reliable climate control and help reduce operational costs. Industrially, they are key to processes requiring precise temperature management—such as drying, dehumidification, and waste heat recovery—and are also found in specialized facilities like food-processing plants and wine cellars. Given their broad range of applications, heat pumps vary considerably in design, capacity, heat/cool sources, and choice of refrigerant.

A heat pump is essentially a thermodynamic device that transfers heat from a lower-temperature source to a higher-temperature reservoir using external energy, typically electricity. It operates on the refrigeration cycle, which involves four main components: (1) a compressor, (2) two heat exchangers (commonly called the condenser and the evaporator), (3) an expansion valve and (4) a working medium, the refrigerant fluid. The refrigerant typically enters the compressor as a low-pressure vapor and exits as a high-pressure, superheated gas. This gas then passes through the condenser, where it releases heat (often via latent heat of condensation) to a cooler fluid or environment (e.g. water) and leaves the condenser as a high-pressure liquid. Next, the expansion valve lowers the fluid’s pressure and temperature at

nearly constant enthalpy. Finally, in the evaporator, the refrigerant absorbs energy from a higher-temperature source (e.g. ambient air) and exits as a low-pressure, superheated vapor, completing the cycle as it returns to the compressor.

2.2 Knudsen Compressor and its porous structure

Taking advantage of the thermal transpiration phenomenon and applying a temperature difference between the edges of a microchannel or porous media under rarefied conditions, where *Kn* is larger than 0.1, mass flow occurs from a low pressure and temperature side to a higher, like a mechanical compressor, by exploiting the thermal creep flow, which is present under vacuum conditions. This setup is often called Knudsen Compressor (KC) or Knudsen Pump and can have practical applications, although currently limited, such as a gas separator [21], a micro-gas chromatography system [22,23], or a motionless heat pump [13-16].

The structure of a Knudsen heat pump (KHP) is similar to conventional heat pumps, consisting of a condenser, an evaporator, an expansion valve or capillary tube and the typical electric drive mechanical pump is substituted by a KC. The benefits of such a device are many. For start a KHP doesn't need the use of classic refrigerants with high values of GWP (Global Warming Potential) and ODP (Ozone Depletion Potential), e.g. R410a, R134a, which harm the environment or flammable and toxic refrigerants, e.g. R290 (Propane), R717 (Ammonia), which can be dangerous for humans. The operating limits of a KHP allow the use of water as the working refrigerant, thus making it an environmentally friendly device. Moreover, there is no need for electricity to power the KHP thus not only minimizing the operating cost, but also giving the opportunity to be used in harsh environments. Although a heat source is needed to heat the one side of the KC, where waste heat from other appliances can be exploited. Also, by substituting the mechanical compressor, there is no part of the heat pump left that is displacing, meaning that this motionless heat pump if free from noise and vibrations. As a result there is no need of lubricant and less need for maintenance. Moreover, by exploiting the structure of the heat pump, many compressors can be connected to series resulting in a multi-stage compressor with increased operating limits and most importantly increased heating/cooling capacity [13,14,16]. The size and capacity of a KHP even with a multi-stage compressor is ranging from 1W up to 2.6kW based on current research models [13,16] and is mainly focused on appliances of small electronic equipment, where the heating loads are critical but they remain relatively low.

In the KHP the Knudsen compressor is actually a porous media and the gas flow is through the porous media due to an established temperature difference between the two end of the porous media. The geometry of porous materials and the way mass flows through them are pivotal to many scientific and industrial applications, from filtration and catalysis to energy storage, biomedical devices, and beyond. By understanding and characterizing pore structures—such as their size distribution, connectivity, and tortuosity—a better prediction and optimization on how fluids or gases traverse these complex networks. Pore sizes in a porous material often follow a distribution—rather than a single uniform value—spanning multiple scales, while tortuosity refers to the free path a fluid must travel through the material which can be characterized as a convoluted channel filled with obstacles rather than a straight line. Many methods have been developed in order to understand the geometry of a porous material like mercury intrusion porosimetry, X-ray tomography, and many models have been proposed which present a correlation between tortuosity and porosity. The most common probably is the Brugemman equation, which was originally proposed for random heterogeneous media [24-26]

$$\tau = \varepsilon^{-0.5} \tag{2.1}$$

where τ is the tortuosity and ε the porosity. Most models, show that as the porosity increases, thus the obstacles a fluid might encounter are less, tortuosity tends to decrease [25-27]. However, other models deduce the opposite behavior [28].

For fibrous porous materials, physical bounds further constrain tortuosity. The lower limit is $\tau = 1$, corresponding to perfectly straight, unobstructed channels; in practice, very open fiber mats ($\varepsilon \gtrsim 0.9$) give τ only slightly above unity (≈ 1.05). As solid loading grows, molecules weave round longer paths. A convenient upper envelope is provided by the geometrical model of Pisani [27],

$$\tau = [1 - \alpha(1 - \varepsilon)]^{-1} \tag{2.2}$$

where the shape factor α is $\approx$ *1.1–1.2* for randomly oriented fibers. This expression predicts $\tau \approx 1.3$ at $\varepsilon \approx 0.80$, rising to $\tau \approx 3$ at $\varepsilon \approx 0.40$. Consequently, the practically attainable window for fiber-based porous media lies in the range $1 \leq \tau \lesssim 3$; higher values can occur in highly compacted, nearly impermeable mats, whereas values below unity are physically impossible.

Moreover, as pore sizes approach micro- and nano-scales, rarefied flow effects become increasingly significant since molecules interact more frequently with the walls than with each other, meaning classical continuum assumptions for fluid transport may break down and require specialized modeling and experimental techniques. Accounting for these rarefied

dynamics is essential in advanced applications like microfluidics, vacuum systems, and gas separation membranes, where ensuring efficient mass transport hinges on accurately capturing the interplay between pore geometry and non-continuum flow behavior.

2.3 Flow configuration

Due to the complexity of porous material and the difficulty to simulate it, for the purpose of this thesis an oversimplified assumption is made, that a porous material can be characterized as a disk which contains many parallel round tubes. Following this assumption the problem of the fully developed flow of a rarefied gas through a long round duct under steady conditions driven by pressure and temperature is considered. The one end of a channel is connected with a large volume at low pressure and temperature while the other with a volume at high pressure and temperature. The flow is from the low pressure towards the high pressure end due to thermal transpiration from the cold volume towards the hot volume. This phenomenon is known as thermal creep. On the other hand a counter flow appears from the high pressure to the low pressure, also known as Poiseuille flow. The net flow of the two phenomena result in a positive flow from the cold to the hot side.

2.4 Linearized Shakhov kinetic model

In order to solve the problem of the flow through a round tube the Shakhov kinetic model is applied. The non-linear Shakhov model with no external force is described by the equation

$$\frac{\partial f}{\partial t} + \tilde{\boldsymbol{\xi}} \cdot \frac{\partial f}{\partial \tilde{\boldsymbol{r}}} = \frac{P}{\mu}(f^S - f) \tag{2.3}$$

Since the flow is steady-state the time derivative is zero and equation (2.3) will become

$$\xi_r \frac{\partial f}{\partial r'} + \xi_\theta \frac{\partial f}{\partial \theta'} + \xi_z \frac{\partial f}{\partial z'} = \frac{P}{\mu}(f^S - f) \tag{2.4}$$

Next, the linearization of the Shakhov model for each problem is described.

2.4.1 Pressure driven flow

For extracting the linear model in a fully developed pressure driven flow a perturbed distribution is introduced as

$$f = f^0\left(1 + h\left(r, \tilde{\boldsymbol{\zeta}}\right)x_P + x_P \frac{z'}{R_t}\right) \tag{2.5}$$

where $h(r,\tilde{\boldsymbol{\zeta}})$ is called perturbation function, $\|x_P\| = \left\|\frac{R_t}{P_0}\frac{dP}{dz'}\right\| \ll 1$ and f^0 is the absolute Maxwellian distribution,

$$f^0 = \frac{N_0}{(2\pi RT)^{3/2}}\, exp\left(-\frac{\xi^2}{2RT_0}\right) \tag{2.6}$$

Next the local Maxwellian is expanded in Taylor series keeping terms up to first order

$$f^M = f^0 + (N - N_0)\left.\frac{\partial f^M}{\partial N}\right|_0 + (\tilde{\boldsymbol{u}} - \tilde{\boldsymbol{u}}_{\boldsymbol{0}})\cdot\left.\frac{\partial f^M}{\partial \tilde{\boldsymbol{u}}}\right|_0 + (T - T_0)\left.\frac{\partial f^M}{\partial T}\right|_0 \tag{2.7}$$

Following some manipulation it is deduced that

$$f^S = f^0\left[\begin{array}{c} 1 + \dfrac{N - N_0}{N_0} + \dfrac{2\tilde{\boldsymbol{\xi}}\cdot\tilde{\boldsymbol{u}}}{2RT_0} + \dfrac{T - T_0}{T_0}\left(\left(\dfrac{\xi}{\sqrt{2RT_0}}\right)^2 - \dfrac{3}{2}\right) \\ + \dfrac{2}{15}\dfrac{m}{N_0(k_BT)^2}\tilde{\boldsymbol{\xi}}\cdot\tilde{\boldsymbol{Q}}\left(\left(\dfrac{\xi}{\sqrt{2RT_0}}\right)^2 - \dfrac{5}{2}\right) \end{array}\right] \tag{2.8}$$

To proceed, in the non-linear model the VDF is replaced by the perturbed distribution

$$\tilde{\boldsymbol{\xi}}\frac{\partial\left[f_0\left(1 + hx_p + x_p\frac{z'}{R_t}\right)\right]}{\partial\tilde{\boldsymbol{r}}} = \frac{P}{\mu}\left(f^S - f^0\left(1 + hx_p + x_p\frac{z'}{R_t}\right)\right) \tag{2.9}$$

After some mathematical manipulation the linearized Shakhov model equation is deduced:

$$\zeta_r\frac{\partial h}{\partial r} = \delta\left[2\zeta_z v_z + \frac{4}{15}\zeta_z q_z\left(\zeta^2 - \frac{5}{2}\right) - h\right] - \zeta_z \tag{2.10}$$

where $\tilde{\boldsymbol{\zeta}} = \frac{\tilde{\xi}}{v_0}, r = \frac{r'}{R_t}, q_z = \frac{Q_z}{v_0 P_0 x_p}, v_z = \frac{u_z}{v_0 x_p}$.

To continue, two projections are introduced which are going to help in the calculations for both the pressure and temperature driven flow. The first projected distribution function is defined as

$$\varphi = \frac{1}{\sqrt{\pi}}\int_{-\infty}^{+\infty}\zeta_z\, he^{-{\zeta_z}^2}d\zeta_z \tag{2.11}$$

Operating accordingly in (2.10) it is deduced that

$$\zeta_r\frac{\partial\varphi_P}{\partial r} = \delta\left[v_z + \frac{2}{15}q_z\left({\zeta_x}^2 + {\zeta_y}^2 - 1\right) - \varphi_P\right] - \frac{1}{2} \tag{2.12}$$

where φ_P is the projection (2.11) referring to the pressure driven flow. The second projected distribution function is defined as

$$\psi = \frac{1}{\sqrt{\pi}}\int_{-\infty}^{+\infty}{\zeta_z}^3\, he^{-{\zeta_z}^2}d\zeta_z \tag{2.13}$$

and operating accordingly in (2.10) it is deduced that

$$\zeta_r \frac{\partial \psi_P}{\partial r} = \delta \left[\frac{3}{2} v_z + \frac{1}{5} q_z \left({\zeta_x}^2 + {\zeta_y}^2 \right) - \psi_P \right] - \frac{3}{4} \tag{2.14}$$

where ψ_P is the projection (2.13) referring to the pressure driven flow The macroscopic velocity is given by

$$u_z = \frac{1}{N} \iiint_{-\infty}^{+\infty} \xi_z f d\tilde{\boldsymbol{\xi}} \tag{2.15}$$

The moments of the VDF are also linearized. More specifically, the bulk velocity becomes

$$u_z = \frac{1}{N} \iiint_{-\infty}^{+\infty} \xi_z \, f_0 \left(1 + h x_p + x_p \frac{z'}{R_t} \right) d\tilde{\boldsymbol{\xi}} = \frac{v_0 x_p}{\pi^{\frac{3}{2}}} \iiint_{-\infty}^{+\infty} \zeta_z \, h e^{-\zeta^2} d\tilde{\zeta} \tag{2.16}$$

In addition, the dimensionless macroscopic velocity $v_{z,P}$ is introduced as

$$v_{z,P} = \frac{u_z}{v_0 x_p} = \frac{1}{\pi^{\frac{3}{2}}} \iiint_{-\infty}^{+\infty} \zeta_z \, h e^{-\zeta^2} d\tilde{\zeta} = \frac{1}{\pi} \int_0^{2\pi} \int_0^{+\infty} \varphi_P \, e^{-{\zeta_r}^2} \zeta_r d\zeta_r d\theta \tag{2.17}$$

$$v_{z,P} = 2 \int_0^{+\infty} \varphi_P \, e^{-{\zeta_r}^2} \zeta_r d\zeta_r \tag{2.18}$$

Similarly, the heat flux given by

$$Q_z = \frac{m}{2} \iiint_{-\infty}^{+\infty} (\xi_z - u_z) \left(\tilde{\boldsymbol{\xi}} - \tilde{\boldsymbol{u}} \right)^2 f d\tilde{\boldsymbol{\xi}} \tag{2.19}$$

is linearized as

$$Q_z = \frac{m}{2} \iiint_{-\infty}^{+\infty} (\xi_z - u_z) \left(\tilde{\boldsymbol{\xi}} - \tilde{\boldsymbol{u}} \right)^2 f_0 (1 + h x_P + x_P) d\tilde{\boldsymbol{\xi}} \tag{2.20}$$

which is rewritten as

$$Q_z = \frac{P_0 v_0 x_P}{\pi^{\frac{3}{2}}} \iiint_{-\infty}^{+\infty} \zeta_z \left(\zeta^2 - \frac{5}{2} \right) h \, exp(-\zeta^2) d\tilde{\boldsymbol{\zeta}} \tag{2.21}$$

The z-component of the dimensionless heat flux $q_{z,P}$ is given by

$$q_{z,P} = \frac{Q_z}{P_0 v_0 x_P} = \frac{1}{\pi^{\frac{3}{2}}} \iiint_{-\infty}^{+\infty} \zeta_z \left(\zeta^2 - \frac{5}{2} \right) h \, exp(-\zeta^2) d\tilde{\boldsymbol{\zeta}} \tag{2.22}$$

and in terms of the projected distributions as

$$q_{z,P} = \frac{1}{\pi}\int_0^{2\pi}\int_0^{+\infty}\left[\psi_P + \left({\zeta_r}^2 - \frac{5}{2}\right)\varphi_P\right] exp\left(-{\zeta_r}^2\right)\zeta_r d\zeta_r d\zeta_\theta \tag{2.23}$$

$$q_{z,P} = 2\int_0^{+\infty}\left[\psi_P + \left({\zeta_r}^2 - \frac{5}{2}\right)\varphi_P\right] exp\left(-{\zeta_r}^2\right)\zeta_r d\zeta_r \tag{2.24}$$

2.4.2 Temperature driven flow (thermal creep flow)

The linearized Shakhov model equation for the temperature driven flow is obtained in a similar manner as the for the pressure driven flow, using the same projections, using however a slightly different definition of the perturbed distribution given by

$$f = f_0\left[1 + hx_T + x_T\frac{z'}{R_t}\left(\frac{\xi^2}{2RT_0} - \frac{5}{2}\right)\right] \tag{2.25}$$

where $\|x_T\| = \left\|\frac{R_t}{T_0}\frac{dT}{dz'}\right\| \ll 1$

The linearized distribution functions are introduced in the non-linear model to yield

$$\tilde{\boldsymbol{\xi}}\frac{\partial\left[f_0\left(1 + hx_T + x_T\frac{z'}{R_t}\left(\frac{\xi^2}{2RT_0} - \frac{5}{2}\right)\right)\right]}{\partial\tilde{r}} = \frac{P}{\mu}\left\{f^S - f_0\left[1 + hx_T + x_T\frac{z'}{R_t}\left(\frac{\xi^2}{2RT_0} - \frac{5}{2}\right)\right]\right\} \tag{2.26}$$

$$\zeta_r\frac{\partial h}{\partial r} = \delta\left[2\zeta_z v_z + \frac{4}{15}\zeta_z q_z\left(\zeta^2 - \frac{5}{2}\right) - h\right] - \zeta_z\left(\zeta^2 - \frac{5}{2}\right) \tag{2.27}$$

Next the projections (2.11) and (2.13) are used in equation (2.27) to get the projected kinetic equations. For the projections (2.11) and (2.13) the final expressions are

$$\zeta_r\frac{\partial\varphi_T}{\partial r} = \delta\left[v_z + \frac{2}{15}q_z\left({\zeta_x}^2 + {\zeta_y}^2 - 1\right) - \varphi_T\right] - \frac{1}{2}\left({\zeta_r}^2 - 1\right) \tag{2.28}$$

and

$$\zeta_r\frac{\partial\psi_T}{\partial r} = \delta\left[\frac{3}{2}v_z + \frac{1}{5}q_z\left({\zeta_x}^2 + {\zeta_y}^2\right) - \psi_T\right] - \frac{3}{4}{\zeta_r}^2 \tag{2.29}$$

respectively. Next, the macroscopic velocity and heat flux for the temperature driven flow are calculated. The macroscopic velocity is linearized as

$$u_z = \frac{1}{N}\iiint_{-\infty}^{+\infty}\xi_z f d\tilde{\boldsymbol{\xi}} = \frac{1}{N}\iiint_{-\infty}^{+\infty}\xi_z f_0\left(1 + hx_T + x_T\frac{z'}{R_t}\left(\frac{\xi^2}{2RT_0} - \frac{5}{2}\right)\right)d\tilde{\boldsymbol{\xi}} \tag{2.30}$$

and is non-dimensionalized as

$$v_{z,T} = \frac{u_z}{v_0 x_T} = 2\int_0^{+\infty} \varphi_T \, e^{-{\zeta_r}^2} \zeta_r d\zeta_r \tag{2.31}$$

Similarly, the heat flux is linearized and non-dimensionalized as

$$Q_z = \frac{m}{2}\iiint_{-\infty}^{+\infty} (\xi_z - u_z)\left(\tilde{\boldsymbol{\xi}} - \tilde{\boldsymbol{u}}\right)^2 f_0 \left(1 + hx_T + x_T \frac{z'}{R_t}\left(\frac{\xi^2}{2RT_0} - \frac{5}{2}\right)\right) d\tilde{\boldsymbol{\xi}} \tag{2.32}$$

$$Q_z = \frac{P_0 v_0 x_T}{\pi^{\frac{3}{2}}} \iiint_{-\infty}^{+\infty} \zeta_z \left(\zeta^2 - \frac{5}{2}\right) h \, exp(-\zeta^2) d\tilde{\boldsymbol{\zeta}} \tag{2.33}$$

$$q_{z,T} = \frac{Q_z}{P_0 v_0 x_T} = 2\int_0^{+\infty} \left[\psi_T + \left({\zeta_r}^2 - \frac{5}{2}\right)\varphi_T\right] exp\left(-{\zeta_r}^2\right)\zeta_r d\zeta_r \tag{2.34}$$

As it seen the expressions of the dimensionless macroscopic velocity and heat flux are the same as for the pressure driven flow but of course the corresponding projected distributions functions are different. Therefore, the results for the macroscopic velocity and heat flux for the temperature driven flow will differ from the pressure driven since the linear models are defined for different perturbed distributions.

2.4.3 Dimensionless flow rates and heat fluxes

For the pressure and temperature driven flows the dimensionless flow rates are given by

$$G_P = 2\pi \int_0^1 v_{z,P} \, r dr \tag{2.35}$$

$$G_T = 2\pi \int_0^1 v_{z,T} \, r dr \tag{2.36}$$

and the corresponding heat flow rates are given by

$$Q_P = 2\pi \int_0^1 q_{z,P} \, r dr \tag{2.37}$$

$$Q_T = 2\pi \int_0^1 q_{z,T} \, r dr \tag{2.38}$$

The kinetic coefficients G_P and Q_T are associated with direct effects, specifically the flow rate and the heat flux generated by pressure and temperature gradients, respectively. In contrast, the coefficients G_T and Q_P arise from cross effects, which vanish as the system moves toward the hydrodynamic regime. The term G_T denotes a flow rate driven by a temperature difference commonly called thermal creep while Q_P describes a heat flux caused by a pressure gradient,

referred to as the mechanocaloric flux. It has been shown in [29–31] that G_T and Q_P satisfy the Onsager–Casimir relation for any scattering kernel that fulfills the reciprocity condition.

2.5 Computation of mass flow rate

To determine the net mass flow rate the kinetic coefficients are applied taking into consideration that the flow is fully developed. Under this admission the flow through a tube can be calculated by the first order ordinary differential equation [32].

$$\frac{dP}{dz} = -\frac{u_0}{\pi R_{ave}^3 G_P(\delta)} \dot{m}_{ch} + \frac{G_T(\delta)}{G_P(\delta)} \frac{P}{T} \frac{dT}{dz} \tag{2.39}$$

At first a database was constructed with the coefficients G_T and G_P for various rarefaction conditions, which would be used later in the model. A practical way to solve the above equation involves an iterative method. First, an initial value for the mass flow is chosen, in this case the one measure in the experiment. Next, equation (2.39) is integrated from the one end of the tube ($z = 0$) to the other ($z = L$), using the known inlet pressure $P(0)$ as the starting condition. The resulting outlet pressure at $P(L)$ is then compared with the experimental measured. If there is a discrepancy, the mass flow estimate is adjusted accordingly, and the process is repeated until the solution converges.

Chapter 3 **EXPERIMENTAL SETUP AND MODELING OF KNUDSEN HEAT PUMP**

The experimental heat pump rig covering the materials, geometry, test parameters, and governing thermodynamic assumptions are described. Also, the numerical model of the Knudsen heat pump, including the Knudsen compressor, which is modeled as an array of parallel micro-channels are predicted.

3.1 Experiment setup and description

The experimental results which have been used in the present work have been obtained at the Department of Micro-Nano Mechanical Science and Engineering at University of Nagoya and Toyota Central R&D Labs and are presented in [13]. It is useful, mainly for completeness purposes, to provide a brief description of the experimental setup.

The experimental Knudsen heat pump is shown in Figure 2.1. It consists of the Knudsen compressor (A), condenser (B) and evaporator (C) all connected with pipes to form a closed system. Cooling water is supplied to the evaporator from the cooling water tank (4) via valve (25). The vacuum pump (5) is connected to the heat pump through valve (27). Between the condenser (B) and the evaporator (C) the expansion valve (26) is placed. In the compressor (A), the porous (1) is a glass fiber filter (Millipore, APFF) with the following characteristics: 0.70μm average pore size, 380μm thickness, 114mm diameter, 773K heatproof temperature, 90% porosity ($\varepsilon = 0.9$). In order to increase the temperature difference through the compressor two filters are stacked and their outer region is adhered to the setup, resulting in a salutary 100mm diameter. The temperature difference through the compressor is imposed with the halogen lamp (3) heating the outlet of the compressor and the heat exchanger (6) cooling the inlet of the compressor. The temperature of the cooling medium in the heat exchanger is controlled (12) and two thermocouples are used for measuring the temperature of the cooling medium and the surface temperature of the filter at the hot side (15 and 16). The evaporator and the condenser consist of a 45mm square copper plate with fine grooves to hold the water (7 and 8) and a Polyether ether ketone (PEEK) manifold. On the

other side of the plates a medium is flowing for heating or cooling the heat exchangers (evaporator and condenser). The temperature of each medium is controlled by the temperature control devices (13 and 14), while thermocouples are installed at the inlet and outlets (17-20). In addition, flow sensors are placed at the outlet (21 and 22). Also, two pressure sensors have been installed in the manifold of each heat exchanger (23 and 24).

The water temperature in both heat exchangers is calculated via Antoine's equation for saturated vapor as

$$\log_{10}(P) = A - \frac{B}{T - C} \tag{3.1}$$

where *P* and *T* are the water vapor pressure (bar) and temperature (K) of water respectively, while the constants *A, B, C* are given in Table 2.1 [33].

Table 3.1: Antoine equation parameters for water

Temperature range (K)	*A*	*B*	*C*
273 - 303	5.40221	1838.675	-31.737
303 – 333	5.20389	1733.926	-39.485
333 – 363	5.0768	1659.793	-45.854
344 – 373	5.08354	1663.125	-45.662

The experiment have been performed for five different temperature setups, where the measured temperatures at the inlet and outlet of the compressor, as well as at the condenser and the evaporator are provided in Table 2.2 (Cases I - V). The inlet temperature of the compressor and the saturation temperatures of the evaporator and condenser in all cases I-V have very small deviations, while the outlet temperature of the compressor varies about 10 degrees from about 487.9 K to 497.8 K.

Table 3.2: Measured temperatures at the heat pump experimental rig [13]

Case	Compressor temperature (K)		Condenser temperature (K)	Evaporator temperature (K)
	Inlet T_{in}	Outlet T_{out}		
I	294.46	497.77	279.12	278.26
II	294.56	488.71	279.17	278.18
III	294.60	488.52	279.22	278.14
IV	294.54	488.03	279.27	278.10
V	294.43	487.93	279.31	278.07

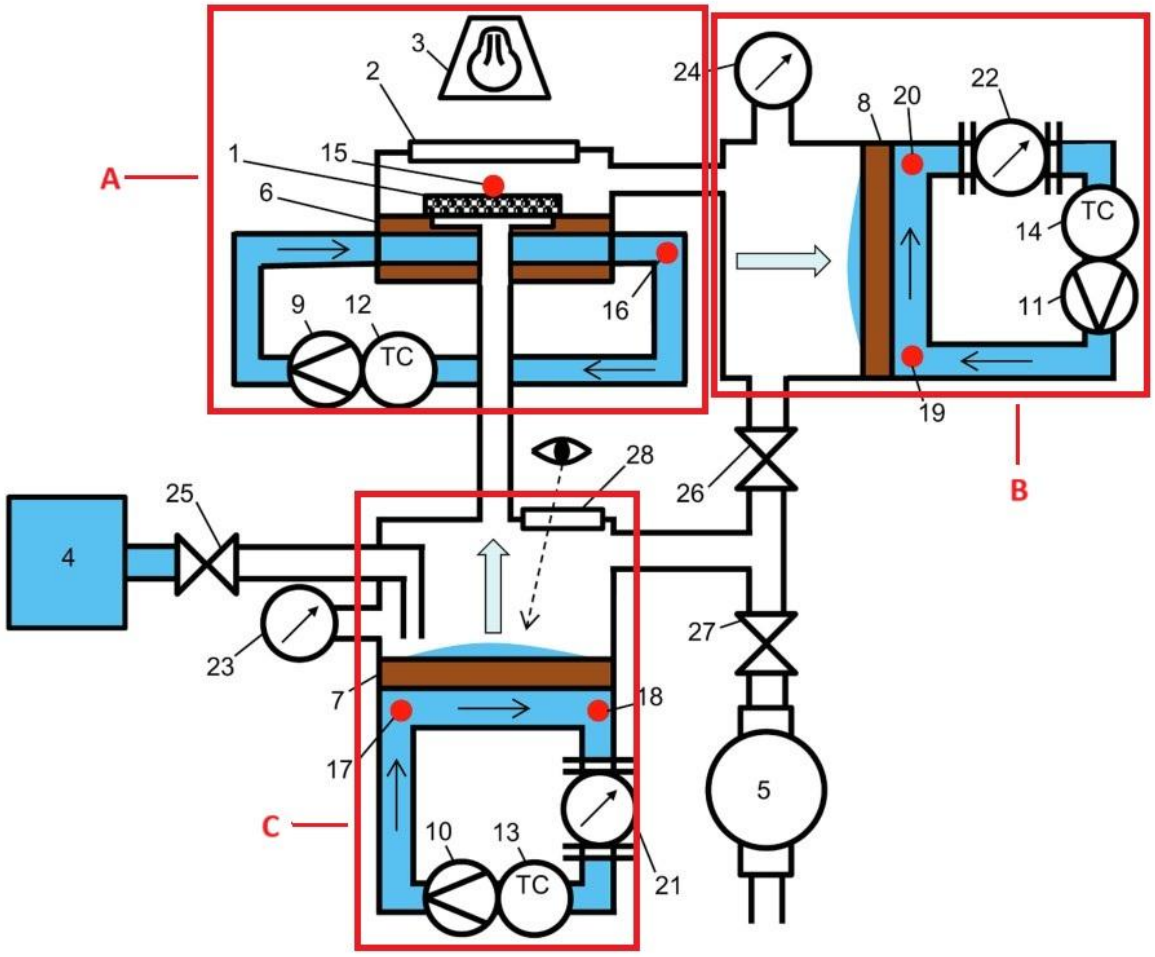

Figure 3.1: Heat pump experimental rig [13]

3.2 Knudsen heat pump modeling

The heat pump model follows the basic principles of the refrigeration cycle and the assumptions made by [13]. As shown in Figure 3.1, it includes isobaric evaporation at evaporator (6→1), isobaric heating from evaporator outlet to KC inlet (1→2), compression through the KC (2→3), isobaric cooling from KC outlet to condenser inlet (3→4), isobaric condensation at condenser (4→5) and adiabatic expansion through the valve (5→6). All four temperatures at the different stages of the cycle have been measured and given in [13] (see also Table 3.2).

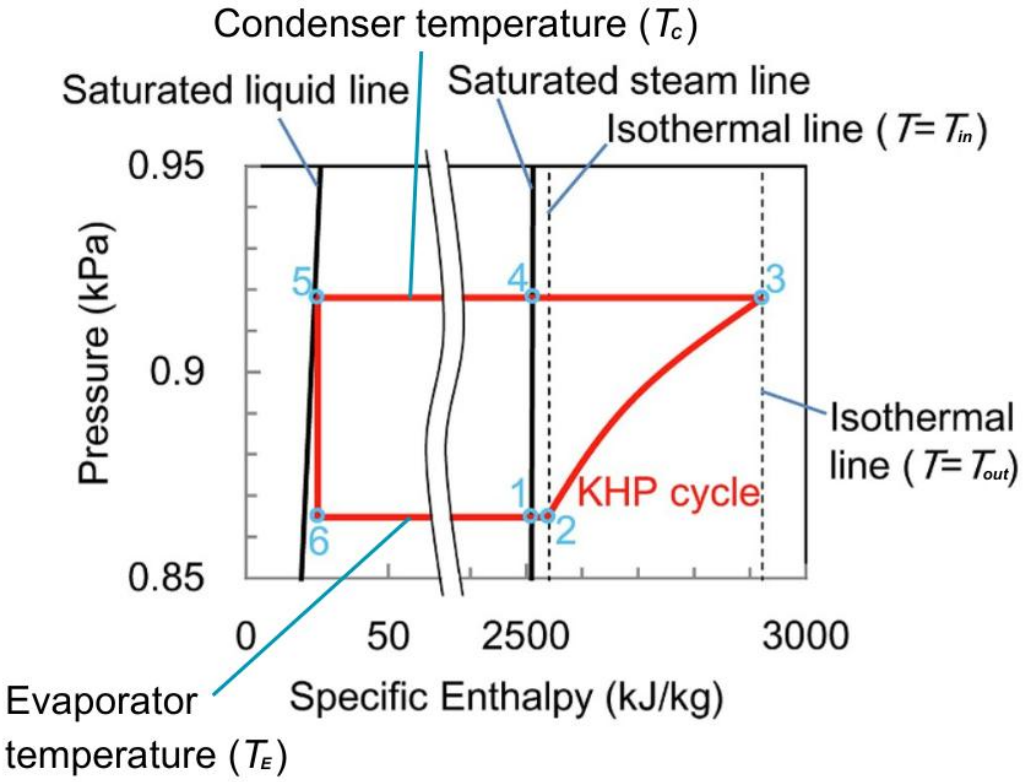

Figure 3.2: Pressure-enthalpy diagram of KHP with operating limits of [13]

Once the Knudsen compressor is modeled and the associates mass flow rate is computed, all variables at each stage of the heat pump can be extracted as follows:

- Compression work $W = \dot{m}(h_3 - h_2)$
- Heat transfer at condenser $Q_C = \dot{m}(h_4 - h_5)$
- Heat transfer at evaporator $Q_E = \dot{m}(h_1 - h_6))$
- Coefficient of performance $COP_{cool} = Q_E/W, COP_{heat} = Q_C/W$

The Knudsen compressor is approximated by a circular disk with length L and area A_{tot} equal to the porous material used in the experiment. The total volume of the porous material is

$$V_{tot} = LA_{tot} \tag{3.2}$$

The disk is assumed to contain a large number of straight parallel circular tubes, N_{ch}, with diameter equal to the average pore diameter of the material, D_{ave} . The total volume of the porous in the material is

$$V_p = \varepsilon \times V_{tot} \tag{3.3}$$

where ε is the porosity of the material. Also, the volume of a single channel is

$$V_{ch} = L\frac{\pi D_{ave}^2}{4} \tag{3.4}$$

and the number of circular tubes is given by the ratio

$$N_{ch} = \frac{V_p}{V_{ch}} \tag{3.5}$$

The specific geometric characteristics of the Knudsen compressor are given in Table 3.3 [13].

Table 3.3 Geometric characteristics of the Knudsen compressor

Compressor diameter	D	*100* mm
Compressor length	L	*760* μm
Compressor area	A_{tot}	*7854* mm^2
Compressor volume	V_{tot}	*5969* mm^3
Porosity	ε	*0.90*
Average pore diameter	D_{ave}	*0.70* μm
Number of channels	N_{ch}	*18.367.346.939*
Single channel volume	V_{ch}	*2.92482E-07* mm^3
Total channel volume	V_p	*5372* mm^2
Tortuosity	τ	*1.00*

Next, using equation (2.39) the mass flow rate for a single channel, $\dot{m}_{ch}$ is calculated as

$$\frac{dP}{dz} = -\frac{u_0}{\pi R_{ave}^3 G_P(\delta)}\dot{m}_{ch} + \frac{G_T(\delta)}{G_P(\delta)}\frac{P}{T}\frac{dT}{dz} \tag{3.6}$$

where $u_0 = \sqrt{2RT}$ is the most probable molecular speed with *R=287.09* J/(kgK) being the specific gas constant of water vapor, P is the pressure along the tube and T is the temperature along the channel wall. The kinetic coefficients G_P and G_T denote the reduced flow rates for

the pressure and temperature driven flows and are functions of the local value of the rarefaction parameter

$$\delta = \frac{PR_{ave}}{\mu u_0} \tag{3.7}$$

where μ is the dynamic viscosity of vapor water.

To extract the mass flow through one channel using equation (3.6) the following parameters are inserted:

- Geometric characteristics of the compressor (average pore radius $R_{ave} = \frac{D_{ave}}{2}$ and channel length *L)*.
- Linear temperature distribution along the wall, based on the inlet and outlet temperatures of the channel ($T_{in} = T_2$ *and* $T_{out} = T_3$ from Table 3.2).
- Pressure at the inlet of the compressor ($P_{in} = P_2 = P_E$).

To continue a shooting method is applied where the mass flow rate $\dot{m}_{ch}$ is assumed to extract the outlet pressure of compressor $P_{out} = P_3 = P_C$. The computed pressure is compared with the experimental pressure P_C, since as noted isobaric cooling from point 3 to 4 (see Figure 3.2). This process is repeated by altering the mass flow rate until there is a match between the calculated and experimental pressure. Then, the total mass flow through the KC is calculated by multiplying the extracted mass flow with the number of channels:

$$\dot{m}_{tot} = N_{ch}\dot{m}_{ch} \tag{3.8}$$

Finally, based on the computed mass flow rate of KC, the output characteristics of the heat pump are calculated.

Chapter 4 **RESULTS AND DISCUSSION**

In this chapter, all Cases I-V are simulated and the computed results are compared to the experimental ones. The simulation is performed by employing the temperatures at the evaporator and condenser, from [13]. It is noted however that in the experimental data are based on the corresponding pressure measurements. Furthermore, in an effort to match the measured and computed heat flows, the simulations are performed following various scenarios. Also, the effects of tortuosity, as well as of small variations in the saturated temperature in the evaporator and condenser are investigated. Finally, a parametric analysis is provided for both the KC and KHP, based on various involved parameters.

4.1 Heat flow rates in evaporator and condenser

As noted above the computed mass flow rate depends on the imposed temperatures at the inlet and outlet of the compressor (T_{in}, T_{out}), as well as on the pressure of the condenser and evaporator (isobaric processes have been assumed, i.e., $P_1 = P_2 = P_E$ and $P_3 = P_4 = P_C$). Thus, the temperatures at condenser and evaporator have also an effect on the computed mass flow rates. More specifically, based on the measured temperatures at the evaporator and condenser the corresponding saturated pressures are readily deduced and since isobaric processes have been assumed, these pressures are the same with the inlet and outlet pressure at the compressor respectively.

Based on the measured temperatures according to Table 3.2 for all Cases I-V, the KC and the KHP models described in Chapter 3 are applied. The computed pressures are provided in Table 4.1, while the associated mass flow rates and heat fluxes are provided in Table 4.2. All results are compared with the corresponding experimental ones [13]. As seen in Table 4.1, the imported condenser and evaporator saturation temperatures ($T_C = T_4$, $T_E = T_1$) and the corresponding saturation pressures (P_C, P_E) are in excellent agreement with the experimental data. Thus, the boundary conditions of the model, more specifically, the imposed temperatures and pressures, are well aligned with those of the physical experiment. The small

deviations between computations and measurements in pressure are due to the fact that in the former case the pressure is deduced from the temperature, while in the latter one pressure is directly measured. In the experiment the pressures at condenser and evaporator are measured using sensors and the respective temperatures are being calculated using Antoine's equation (3.1). The numerical mode on the other hand uses as input the temperature at evaporator and condenser, given by [13], and the respective saturation state and calculates the pressure based on the thermodynamic properties of water. For that reason pressures are presented in the following tables as output.

As seen however, in Table 4.2, significant discrepancies exist between the computed mass flow ($\dot{m}$) and heat fluxes at the condenser (Q_C) and evaporator (Q_E). For all three quantities the deviations are about 30% in Case I, then they increase up to about 60% and 100% in Cases II and III respectively and finally, they become even higher than 100% in Cases IV and V. The numerical results always exceed the experimental measurements, suggesting that certain geometrical and/or physical effects in the experiment are missed or simplified in the model. Potential contributors to this mismatch include the unaccounted thermal losses through the system walls, differences in material properties or surface conditions and assumptions regarding flow regimes that may not hold across all operating conditions. Of course, measurement errors may also be present. For example, it is noted that in the numerical results, always $Q_C > Q_E$, as it should be, due to the first law of thermodynamics. However, in the experimental data, in Cases I, II and III, $Q_C < Q_E$, while in Cases IV and V, $Q_C > Q_E$. Another issue related to experimental errors are the reported uncertainties, where in Cases I-IV they range from 8-14%, while in Case V they reach 45%.

Table 4.1: Comparison of P_E, P_C and ΔT_{HP} (inputs: T_E and T_C, with $\tau=1$)

Case	T_E (K)	T_C (K)	P_E (Pa)		P_C (Pa)		ΔT_{HP} (K)	
			Present	[13]	Present	[13]	Present	[13]
I	278.26	279.12	879.29	876	933.41	930	0.860	0.859 ± 0.004
II	278.18	279.17	874.40	871	936.65	933	0.990	0.990 ± 0.004
III	278.14	279.22	871.97	868	939.89	936	1.080	1.084 ± 0.004
IV	278.10	279.27	869.54	866	943.15	939	1.170	1.166 ± 0.005
V	278.07	279.31	867.72	864	945.76	942	1.240	1.240 ± 0.005

Table 4.2: Comparison of Q_E , Q_C and $\dot{m}$ (inputs: T_E and T_C, with $\tau=1$)

Case	Q_E (W)			Q_C (W)			$\dot{m}$ (kg/s)		
	Present	[13]	%	Present	[13]	%	Present	[13]	%
I	4.018	3.09 ± 0.31	30	4.021	2.88 ± 0.26	40	1.62E-6	1.24E-6	31
II	3.688	2.37 ± 0.18	56	3.691	2.35 ± 0.22	57	1.48E-6	9.42E-7	57
III	3.543	1.78 ± 0.31	99	3.546	1.58 ± 0.22	124	1.43E-6	7.08E-7	102
IV	3.396	1.07 ± 0.18	217	3.399	1.53 ± 0.18	122	1.37E-6	4.25E-7	222
V	3.289	0.53 ± 0.23	521	3.292	0.78 ± 0.18	322	1.32E-6	2.11E-7	526

Figure 4.1 provides some further insight into these discrepancies by examining how the heat transfer at evaporator and condenser (Q_C, Q_E) changes with the temperature difference ΔT_{HP} between condenser and evaporator ($\Delta T_{HP} = T_C - T_E$). Although both the model and the experiment exhibit an almost linear decrease of Q_C and Q_E as ΔT_{HP} increases, the numerical curve slope is substantially smaller than the experiment one. The model predicts an average slope of about -5% for both heat exchangers, whereas the experimental data show a slope of approximately -25% and -35% for the condenser and evaporator respectively. These results imply that the numerical model underestimates the system sensitivity to larger temperature differences between condenser and evaporator, pointing out the need for more detailed modeling of the internal heat and mass transfer processes, the potential phase-change dynamics and the impact of rarefied flows within the Knudsen compressor.

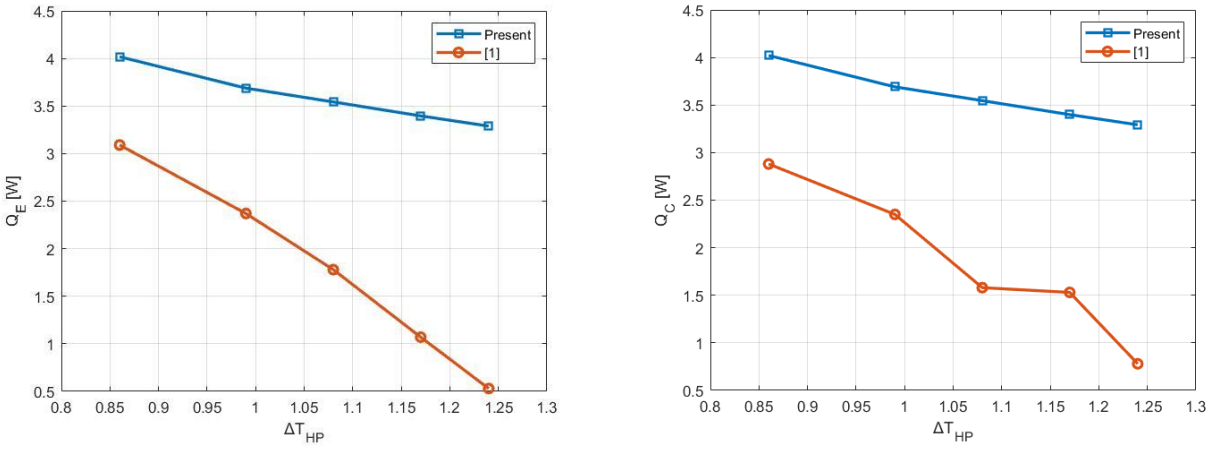

Figure 4.1: Heat transfer of evaporator and condenser vs temperature difference ΔT_{HP}.

Due to the considerable discrepancies between the computed and measured heat fluxes, an alternative modeling approach has been adopted, based on Eq. (3.6). Now, the experimental mass flow rate ($\dot{m}$) is prescribed as input, while the outlet pressure ($P_{out} = P_C$) is computed. All other parameters, i.e., the geometric characteristics (R_{ave}, L), the inlet pressure ($P_{in} = P_E$) and the temperature difference in the compressor (T_{in}, T_{out}) remain the same. The results are provided in Tables 4.3 and 4.4.

As shown in Table 4.3, now the deviations between the computed and measured condenser pressure P_C vary from 5% in Case I up to 14% in Case V. Although the variations may seem small they deduce erroneous condenser temperatures T_C and, as shown in Table 4.4, significant discrepancies in temperature difference ΔT_{HP}. The computed ΔT_{HP} is about the double of the experimental ones. However, now, as seen in Table 4.4, by fixing the mass flow rate to be equal to the experimental ones, the heat transfer in the evaporator (Q_E) and condenser (Q_C) closely aligns with the experimental values.

These findings suggest that, although specifying inlet pressure and mass flow rate, may improve the prediction of the heat transfer in the heat pump, additional refinements are necessary to address the remaining errors in temperature and pressure. Thus, although certain outputs benefit from this approach, the overall model still requires more comprehensive adjustments to fully capture the complex physics governing the Knudsen heat pump performance. This is considered in the next subsection by modifying the tortuosity.

Table 4.3: Comparison of T_C, P_C (inputs: T_E and $\dot{m}$, with $\tau=1$)

Case	T_E (K)	$\dot{m}$ (kg/s)	T_C (K)		P_C (Pa)		
			Present	[13]	Present	[13]	%
I	278.26	1.24E-6	279.76	279.12	975.790	930	5
II	278.18	9.42E-7	280.08	279.17	997.303	933	7
III	278.14	7.08E-7	280.41	279.22	1020.223	936	9
IV	278.10	4.25E-7	280.81	279.27	1048.506	939	12
V	278.07	2.11E-7	281.11	279.31	1070.290	942	14

Table 4.4: Comparison of ΔT_{HP}, Q_E and Q_C (inputs: T_E and $\dot{m}$, with $\tau=1$)

Case	ΔT_{HP} (K)		Q_E (W)		Q_C (W)	
	Present	[13]	Present	[13]	Present	[13]
I	1.503	0.859 ± 0.004	3.078	3.09 ± 0.31	3.082	2.88 ± 0.26
II	1.900	0.990 ± 0.004	2.337	2.37 ± 0.18	2.340	2.35 ± 0.22
III	2.272	1.084 ± 0.004	1.756	1.78 ± 0.31	1.758	1.58 ± 0.22
IV	2.711	1.166 ± 0.005	1.053	1.07 ± 0.18	1.055	1.53 ± 0.18
V	3.043	1.240 ± 0.005	0.523	0.53 ± 0.23	0.524	0.78 ± 0.18

4.2 Channel tortuosity effect

The initial model treated the Knudsen compressor channels as straight tubes, with tortuosity $\tau = 1$. Here, an attempt is made to investigate the effect of this assumption by changing the tortuosity of the channel. To address this limitation, tortuosity τ is introduced in the model by increasing the channel length and reducing the total number of flow paths, both of which act to decrease the mass flow rate. This channel elongation is in the right direction since the computed mass flow rates are always larger than the experimental ones. As a consequence Eq. (3.3) becomes:

$$V_{ch} = L_\tau \frac{\pi D_{ave}^2}{4} \tag{4.1}$$

where,

$$L_\tau = \tau L \tag{4.2}$$

Firstly, the tortuosity is computed by the Brugemman expression (2.1), where for porosity $\varepsilon = 1$, the tortuosity is $\tau = 1.054$. This value is very close to $\tau = 1$, which has been used in the results presented in Section 4.1 (straight channels) and therefore, the reduction of the mass flow is expected to be small. Secondly, another larger value has been searched by trial and error. The selected one is based on the Pisani expressions (2.2) with $\varepsilon \approx 0.8$ to deduce $\tau = 1.3$ and produces reasonably good agreement between computations and measurements in Cases I, II and III. Results have been obtained by using both approaches, i.e., by employing the experimental a) condenser pressures and b) mass flow rates.

In the first scenario, all experimental temperatures and pressures are provided in the model. In Tables 4.5 and 4.6 the computed heat flows and mass flow rates respectively are provided for $\tau = 1.054$ and $\tau = 1.3$, along with the corresponding experimental results. It is noted that the values of T_E, T_C, P_E, P_C and ΔT_{HP} are similar with the ones in Table 4.1 and

therefore are not presented here. For $\tau = 1.054$ the decrease in the mass flow rate and the heat fluxes, compared to the previous case with $\tau = 1$, is rather small (about 7%) and there is no significant improvement in the comparison between computations and measurements. However, for $\tau = 1.3$ all quantities are reduced about 32% with regard to the computed ones with $\tau = 1$ and now, they are much closer to the experimental ones. Now the deviations in Cases I and II are about 10%, about 50% in Case III and they remain high, but not as large as before, in Case IV and V. It may be argued that the porosity and the tortuosity of the channel is an important factor, which may significantly affect the computational model.

Table 4.5: Comparison of Q_E and Q_C with varying tortuosity (inputs: T_E and T_C)

Case	Q_E (W)			Q_C (W)		
	Present τ =1.054	Present τ =1.3	[13]	Present τ =1.054	Present τ =1.3	[13]
I	3.722	2.722	3.09 ± 0.31	3.724	2.724	2.88 ± 0.26
II	3.416	2.499	2.37 ± 0.18	3.418	2.500	2.35 ± 0.22
III	3.282	2.400	1.78 ± 0.31	3.284	2.402	1.58 ± 0.22
IV	3.145	2.300	1.07 ± 0.18	3.148	2.302	1.53 ± 0.18
V	3.047	2.228	0.53 ± 0.23	3.049	2.230	0.78 ± 0.18

Table 4.6: Comparison of $\dot{m}$ with varying tortuosity (inputs: T_E and T_C)

Case	$\dot{m}$ (kg/s)			
	Present τ =1.00	Present τ =1.054	Present τ =1.3	[13]
I	1.62E-6	1.50E-06	1.10E-06	1.24E-6
II	1.48E-6	1.37E-06	1.01E-06	9.42E-7
III	1.43E-6	1.32E-06	9.66E-07	7.08E-7
IV	1.37E-6	1.27E-06	9.26E-07	4.25E-7
V	1.32E-6	1.23E-06	8.97E-07	2.11E-7

In the second scenario, the mass flow rate is defined along with the other parameters in the model but the outlet compressor pressure is calculated. In Tables 4.7 and 4.8, the computed temperature and pressure of the condenser and the temperature difference ΔT_{HP} respectively are provided for $\tau = 1.054$ and $\tau = 1.3$, along with the corresponding

experimental results. It is noted that the values of Q_E, Q_C, T_E and P_E are similar with the ones in Tables 4.3 and 4.4 and therefore are not presented here. As expected the condenser temperature and pressure, as well as temperature difference ΔT_{HP} decrease as tortuosity increases. In general the computational results for $\tau = 1.3$, compared to the ones with $\tau = 1.054$ or $\tau = 1$, are always closer to the experimental ones, but still they do not manage to satisfactory approach the experimental results in all cases. In Case I for $\tau = 1.3$ the compressor outlet pressure is smaller than the condenser pressure. This is not possible as there is no mechanism to increase the pressure between the two stages. The only reasonable explanation would be that the experimental measurement is wrong. This remark is supported by the numerical value of ΔT_{HP}, which is half compared to the experimental one. Case II provides the better results in terms of P_C and ΔT_{HP}, while Cases III-V still produce temperature differences ΔT_{HP} significantly larger than the experimental ones.

Table 4.7: Comparison of T_C and P_C with tortuosity (inputs: T_E and $\dot{m}$)

Case	T_C (K)			P_C (Pa)		
	Present τ =1.054	Present τ =1.3	[13]	Present τ =1.054	Present τ =1.3	[13]
I	279.597	278.744	279.12	964.672	909.417	930
II	279.957	279.331	279.17	988.900	947.128	933
III	280.321	279.863	279.22	1013.906	982.495	936
IV	280.758	280.492	279.27	1044.713	1025.853	939
V	281.087	280.958	279.31	1068.406	1059.039	942

Table 4.8: Comparison of ΔT_{HP} with tortuosity (inputs: T_E and $\dot{m}$)

Case	ΔT_{HP} (K)		
	Present τ =1.054	Present τ =1.3	[13]
I	1.337	0.484	0.859 ± 0.004
II	1.777	1.151	0.990 ± 0.004
III	2.181	1.723	1.084 ± 0.004
IV	2.658	2.392	1.166 ± 0.005
V	3.017	2.888	1.240 ± 0.005

4.3 Evaporator and condenser temperature effect

Based on the previous results it is realized that very small changes in the temperature (and pressure) of the evaporator and condenser deduce large changes on the mass flow rates and heat fluxes. Thus, a parametrization study is performed to investigate the effect of the evaporator and condenser temperatures, while the tortuosity remains constant at $\tau = 1$. More specifically, it is attempted to minimize the error of both heat flows Q_E and Q_C by changing the temperature data T_E, and T_C at the evaporator and condenser respectively. The study includes all cases I-V and the temperature range that has been examined is ± 1.5 degrees with respect to the experimental temperatures, with a step of 0.05 degrees. This is a long parametrization exercise and in each of the five cases considered, the evaporator and condenser temperatures providing the optimum results are selected based on the following criteria: $\min(\left|Q_{C_{exp}} - Q_{C_{comp}}\right| + \left|Q_{E_{exp}} - Q_{E_{cpmp}}\right|)$

In Table 4.9 the optimum condenser and evaporator temperatures are provided along with the corresponding experimental data in [13], while in Table 4.10, the associated computational and experimental heat flows and mass flow rates are tabulated. It is evident that very small deviations in temperature, namely less than -0.25% (or 0.7 degrees) in T_E and +0.25% in T_C, yield significant changes in the heat flows and provide results with very good agreement with the experimental ones. More specifically, the discrepancies with [13], in Cases I, II and III are less than 11% and in Case IV less than 21% and only in Case V remain relatively high, but this is a case with the very large experimental uncertainties.

It is noted that the optimum numerical temperatures in Table 4.09 are always higher than the experimental ones at the condenser and always lower at the evaporator. This implies that heat transfer is not as efficient as it is supposed to be in both heat exchangers. The results in Tables 4.9 and 4.10 reveal the need of high accuracy in the measurement of all operating temperature and pressures in order to properly model the KHP, since very small deviations in the measured temperatures result in large changes in the heat flows and mass flow rates.

Table 4.9: Deviation of T_C and T_E

Case	T_E (K)			T_C (K)		
	Present	[13]	%	Present	[13]	%
I	277.66	278.26	-0.22	279.22	279.12	0.04
II	277.68	278.18	-0.18	279.52	279.17	0.13
III	277.44	278.14	-0.25	279.77	279.22	0.2
IV	277.40	278.1	-0.25	279.97	279.27	0.25
V	277.37	278.07	-0.25	280.01	279.31	0.25

Table 4.10: Comparison of Q_C, Q_E and $\dot{m}$ for alternate temperatures T_C and T_E

Case	Q_E (Pa)			Q_C (Pa)			$\dot{m}$ (kg/s)		
	Present	[13]	%	Present	[13]	%	Present	[13]	%
I	2.88	3.09	6.88	2.88	2.88	0	1.16E-06	1.24E-06	6.57
II	2.35	2.37	0.92	2.35	2.35	0	9.46E-07	9.42E-07	0.42
III	1.58	1.78	11.05	1.59	1.58	0.38	6.38E-07	7.08E-07	9.86
IV	1.21	1.07	13.15	1.21	1.53	20.72	4.88E-07	4.25E-07	14.85
V	1.10	0.53	108.28	1.11	0.78	41.8	4.45E-07	2.11E-07	111

Finally, in Table 4.11, a comparison is performed between the mass flow rate, in Table 4.10 and the one in Table 4.2 (Section 4.1), where T_C and T_E match the experimental ones. The experimental mass flow rates are also included. Once again, it is emphasized that the mass flow rates (and the heat fluxes) are rapidly change with very small changes in temperatures. Based on the above, it may be argued that small deviations in the temperature at other parts of the heat pump cycle (e.g., T_4 and T_1) may also have major impact on the computed heat flows and mass flow rates.

Table 4.11: Comparison of computed values of $\dot{m}$

Case	$\dot{m}$ (kg/s)		
	Present T_E and T_C according to [1]	Present T_E and T_C according to Table 4.9	[1]
I	1.62E-6	1.16E-06	1.24E-06
II	1.48E-6	9.46E-07	9.42E-07
III	1.43E-6	6.38E-07	7.08E-07
IV	1.37E-6	4.88E-07	4.25E-07
V	1.32E-6	4.45E-07	2.11E-07

4.4 Parametric analysis

A parametric analysis on the impact of various parameters on the performance of the Knudsen compressor (KC) and the Knudsen heat pump (KHP) is presented. This analysis has been originally presented in an internal laboratory report [20] and here it is extended to some other parameters. The original analysis is also included for completeness purposes.

4.4.1 Knudsen compressor

Concerning the performance of the KC, six parameters, namely the channel length and diameter, the porosity of the porous material, the inlet pressure and the compressor inlet pressure and temperature difference between the inlet and outlet of the compressor, have been examined. The inlet temperature is always fixed at $T_{in} = 293.15K$. The reference parameters have been chosen to be the same or close to the experimental ones as follows:

- $L = 0.76mm$
- $D = 0.1m$
- $Porosity = 0.9$
- $P_{in} = 1000Pa$
- $\Delta T = 200K$.

In the parametrization study the above parameters are tested and each time one out of the five parameters is varied, while the remaining four are kept constant.

The parametrization results, as described by the KC performance curves ΔP vs $\dot{m}$, are shown in Fig. 4.2. Overall, the curves exhibit a monotonic linear decrease in pressure difference as the mass flow rate increases, with the maximum pressure difference always occurring at zero flow.

More specifically, a longer channel tends to produce a steeper slope, indicating a more rapid decline in pressure difference with increased flow rate due to the enhanced flow resistance along the extended pathway. Also, the reduction of the channel length helps in the increase of the mass flow rate, particularly at low pressure difference. Similarly, variations in porosity reveal that a higher porosity facilitates a larger mass flow for a given pressure difference, taking into consideration that as porosity decreases the total amount of channels permitting the gas flow through is reduced. On the contrary, as diameter increases the slope starts to become steeper and also the mass flow rate reduces.

Concerning, the two operating conditions, inlet pressure and temperature difference, both have similar effect on the KC. Adjustments in inlet pressure primarily affect the intercept of the curves: higher inlet pressures result in a greater initial pressure difference. Moreover, as the inlet pressure increases so does the mass flow rate. Finally, increasing the temperature difference elevates the curves, reflecting the enhanced thermal transpiration effects that drive a greater pressure build-up under a larger thermal gradient.

4.4.2 Knudsen heat pump

The parametrization analysis of the KHP is performed in terms of the same quantities as the KC. Now the simulations results depict the relationship between the heat transfer at the evaporator (Q_E), the coefficient of performance (*COP*) and the overall efficiency of the KHP (η_{eff}) always with regard to the temperature difference between condenser and evaporator (ΔT_{HP}).

In Fig. 4.3, the parametrization study of Q_E is shown. In all cases, Q_E linearly decreases as ΔT_{HP} increases. This behavior indicates that while a modest temperature difference effectively drives thermally induced flow in the Knudsen compressor, larger ΔT_{HP} amplifies flow resistance or other losses, thereby diminishing net heat transfer in the evaporator. Changes in compressor geometry (length or diameter) illustrate a balance between flow resistance and rarefied gas effects. Smaller diameters and longer channels can enhance thermal transpiration at low ΔT_{HP}, but the resulting flow restriction becomes more significant as ΔT_{HP} increases. Conversely, larger diameters and shorter channels reduce resistance, allowing for higher throughput, but they can diminish the beneficial rarefied effects needed to sustain efficient thermal transpiration. Similarly, variations in inlet pressure and porosity reveal that higher pressures or more open pore structures improve mass flow rate initially, raising Q_E. However, once beyond a certain threshold, the underlying Knudsen mechanisms may be weakened by excessive gas density or insufficient wall interactions, causing the benefit to plateau or even reverse as ΔT_{HP} grows. Adjusting the imposed temperature gradient further demonstrates how an increased driving force boosts Q_E at lower ΔT_{HP}, but also leads to steeper declines under more extreme temperature differences, reflecting the heightened interplay of flow resistance and potential non-ideal effects.

In Fig. 4.4, the parametrization study of *COP* is shown. The coefficient of performance is defined as

$$COP = \frac{Q_E}{W} = \frac{\dot{m}(h_1 - h_6)}{\dot{m}(h_3 - h_2)} \tag{4.3}$$

where W is the output work of the KC, $\dot{m}$ the mass flow and h is the enthalpy on the respective stages. In commercial heat pumps the heat flows at evaporator and condenser usually have a discrepancy and as a consequence the COP is also distinguished in heating and cooling. Here, these deviations are negligible (Sections 4.1-4.3) and therefore, only a single *COP*, the one of the evaporator, is presented.

Similar to Q_E, the coefficient of performance *COP* decreases as ΔT_{HP} increases but at a smaller rate, indicating that while moderate temperature differences effectively drive

thermally induced flow in the Knudsen compressor, larger ΔT_{HP} values amplify flow resistance or introduce other nonideal effects. Concerning the geometry and the structure of the porous material (length, diameter, porosity), their influence on *COP* seems to be negligible as the corresponding curves are overlapping each other. These parameters have a significant effect on the evaporator heat flow rate (see Fig. 4.3). However, this effect is due to the associated changes in the mass flow rate, which is also present and equally affects the output work and therefore the ratio Q_E/W, i.e., the *COP* remains unaffected. Regarding inlet pressure and temperature difference between the inlet and outlet of the compressor, they both affect *COP*. More specifically, COP increases as either P_{in} or ΔT decrease. The influence of the pressure inlet is much smaller compared to the temperature difference.

It should be noted that the *COP* presented in Figure 4.4 ranges around 6.5, a value which is much larger than the ones in typical commercial heat pumps. It is noted that *COP* is used in this specific form at commercial heat pumps because there is no other power input or losses. In the KHP this is not the case since apart from the work needed to maintain the constant temperature difference at the inlet and outlet of the compressor, there are loses due to radiation and conduction from the hot side of the KC to the room and the porous material, respectively. These loses can be expressed as

$$U_{rad} = \sigma A \varepsilon (T_H^4 - T_R^4) \tag{4.4}$$

$$U_{cond} = \frac{kA}{L}(T_H - T_L) \tag{4.5}$$

where σ is the Stephan-Boltzmann constant, ε is the emissivity, T_R is the room temperature and k is the thermal conductivity of porous material. By combining the above loads with the work of the KC the overall efficiency of the KHP η_{eff} is introduced:

$$U_{tot} = U_{rad} + U_{cond} + W \tag{4.6}$$

$$\eta_{eff} = \frac{Q_E}{U_{tot}} \tag{4.7}$$

In Fig. 4.5, the parametrization study of η_{eff} is shown. In all cases η_{eff} <1, i.e. it is significantly lower than *COP* 6.5 (see Fig. 4.4), meaning that the required total input load is much larger than the one in the compressor. Also, the maximum available temperature difference ΔT_{HP} drops close to 3.5, as it does in Figure 4.3, showing again that there is a limit to the effective temperature difference between evaporator and condenser. The behavior of η_{eff} regarding length, porosity and inlet pressure variations is similar to Q_E. However, capillary diameter variations seem to have no effect on overall efficiency. Finally, decrease of the

temperature difference ΔT for $\Delta T_{HP} < 1.3$ results in larger values of efficiency, while for $\Delta T_{HP} > 1.3$, the impact of ΔT is reversed, i.e., results in larger values of efficiency.

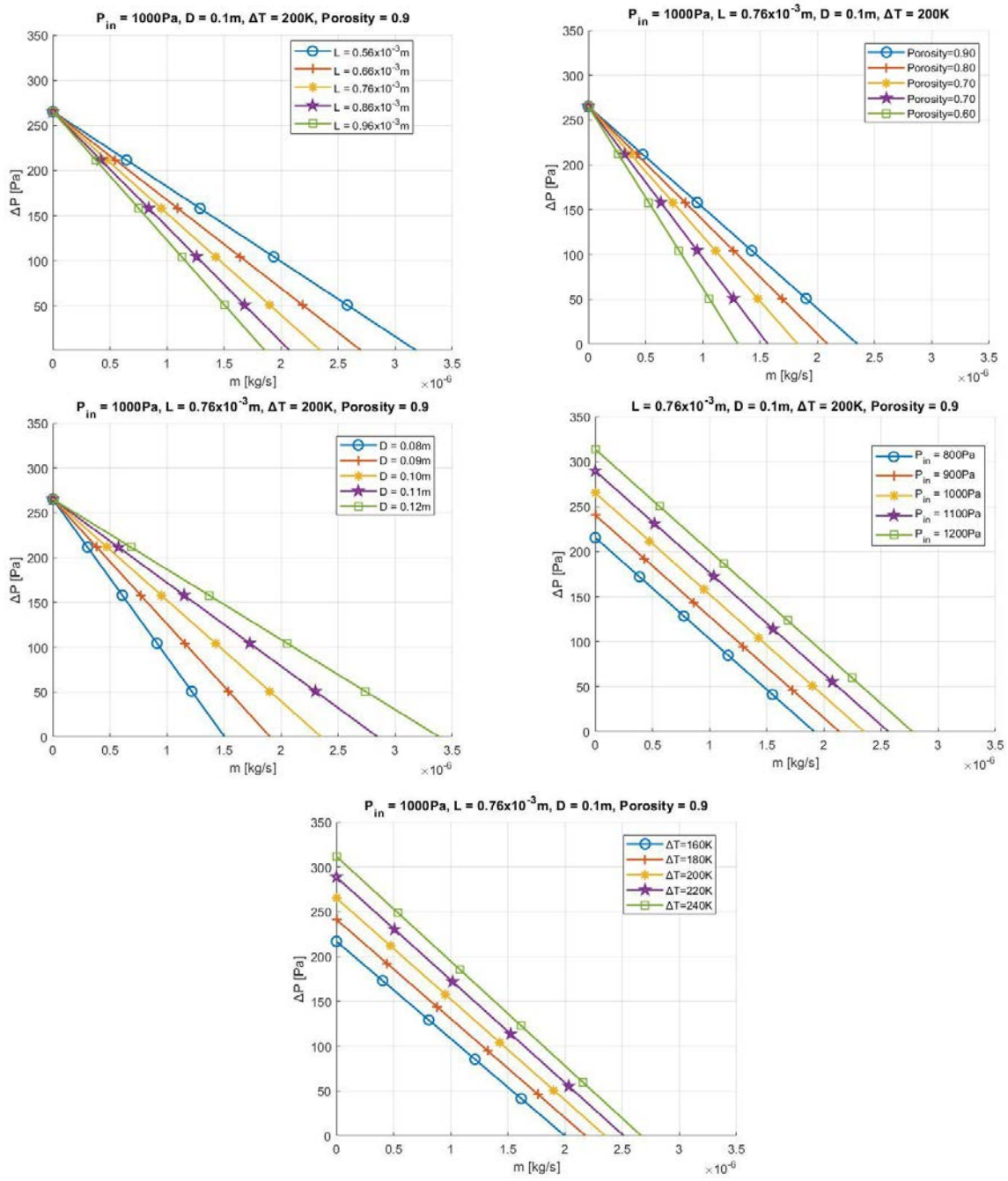

Figure 4.2: Parametric analysis of KC based on a) channel length b) porosity c) diameter d) inlet pressure e) temperature difference ΔT

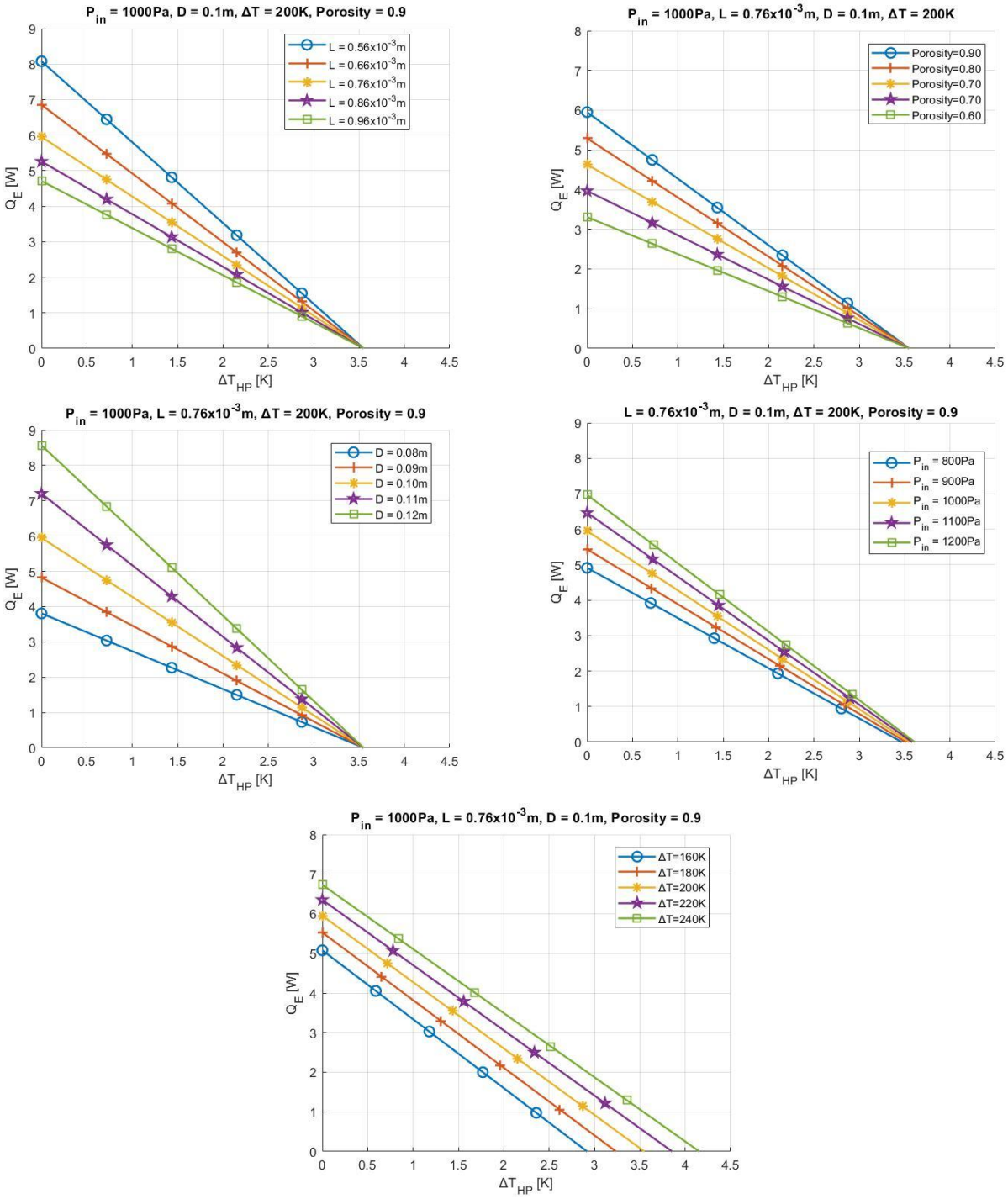

Figure 4.3: Parametric analysis of evaporator heat flow Q_E at the KHP based on a) length b) porosity c) diameter d) inlet pressure e) temperature difference ΔT

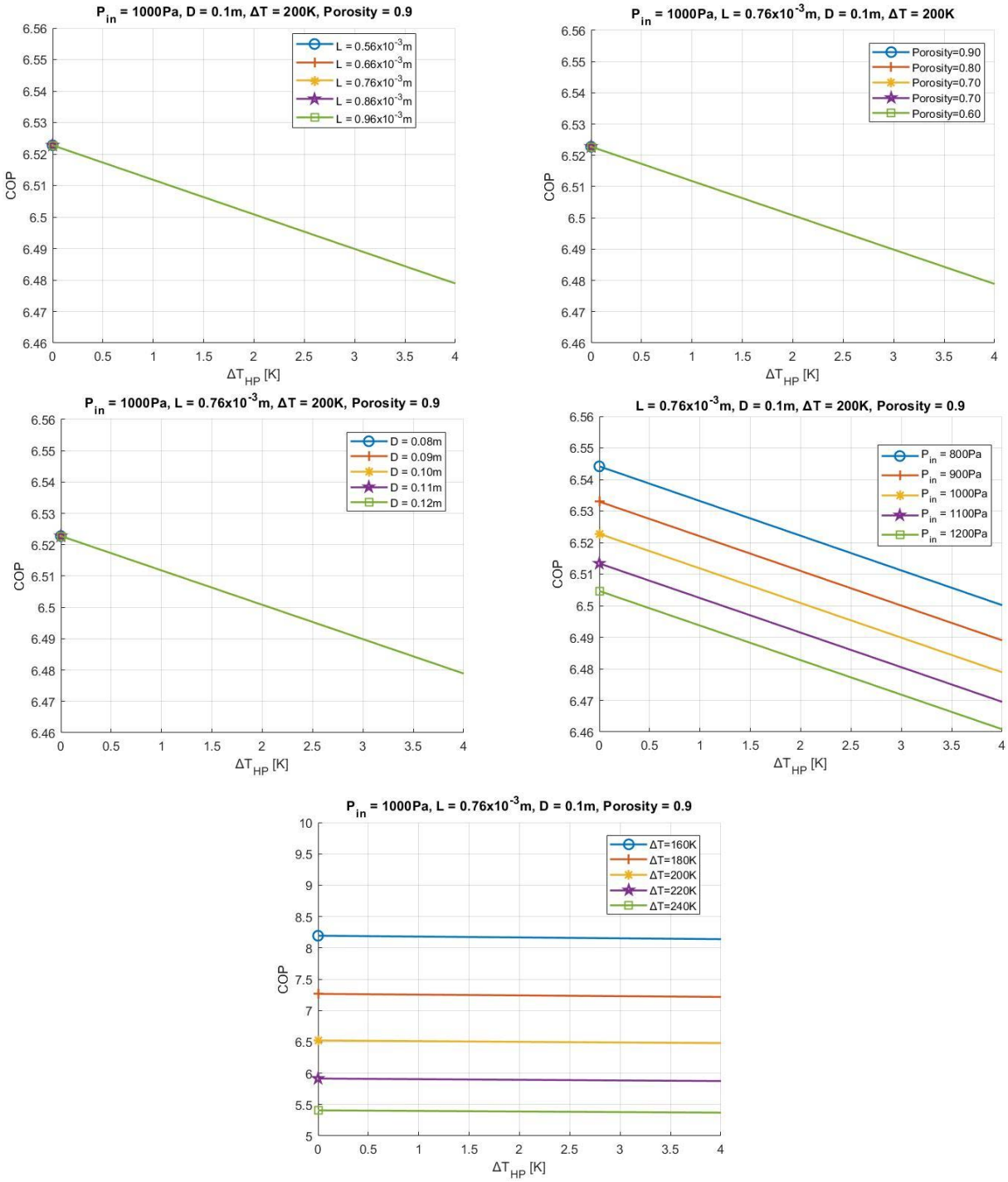

Figure 4.4: Parametric analysis of *COP* of the KHP based on a) length b) porosity c) diameter d) inlet pressure e) temperature difference ΔT

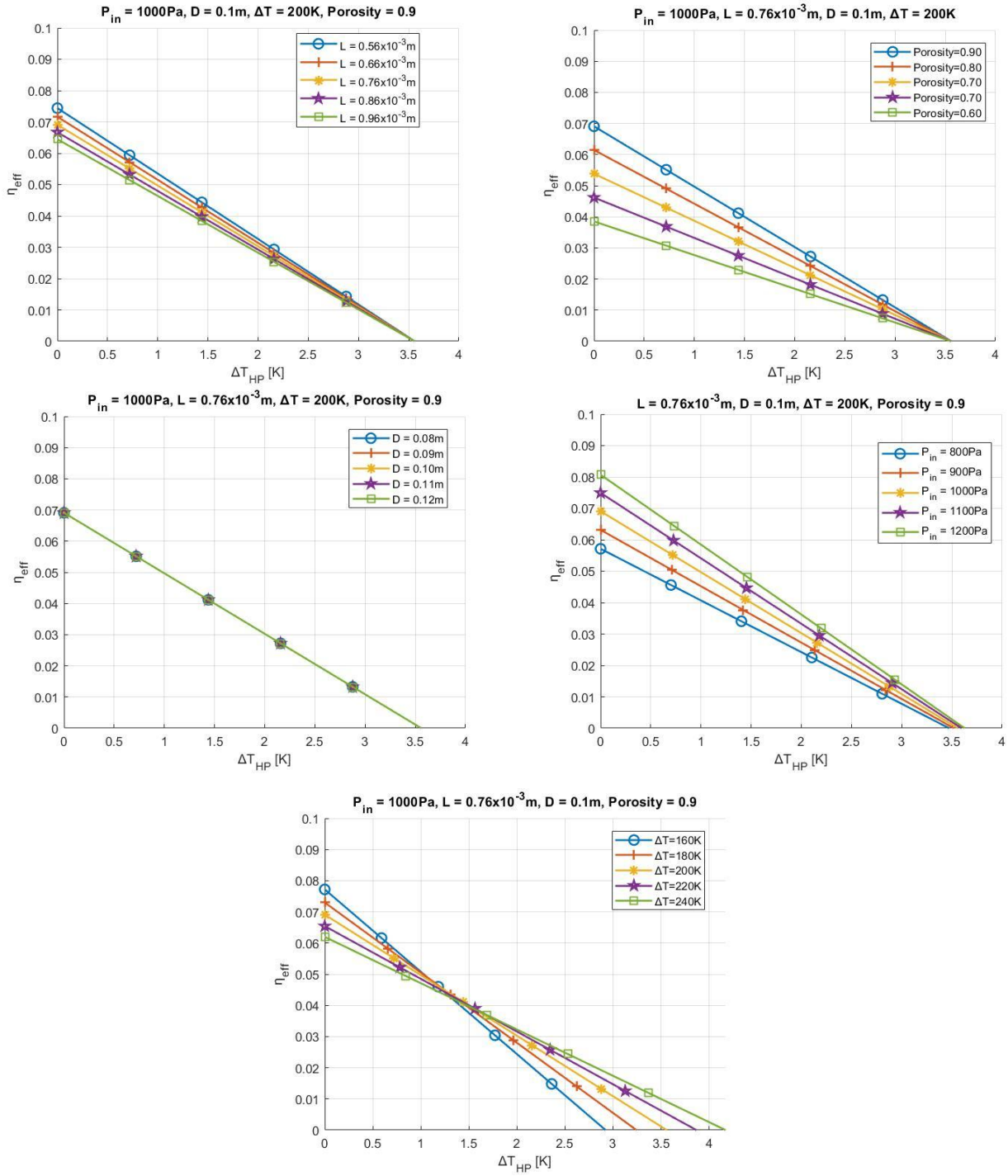

Figure 4.5: Parametric analysis of η_{eff} of the KHP based on a) length b) porosity c) diameter d) inlet pressure e) temperature difference ΔT

Chapter 5 **CONCLUDING REMARKS**

Summing up, this thesis provided a detailed computational analysis of the so-called Knudsen Heat Pump (KHP), emphasizing the potential of integrating a Knudsen compressor in micro-scale heat pump applications. The KHP operates as a typical heat pump, but the compressor has been replaced by a Knudsen compressor, where gas compression is achieved via the thermal transpiration (or thermal creep) phenomenon and therefore, the pressure conditions must be accordingly rarefied.

Here, the experimental KHP developed at the Department of Micro-Nano Mechanical Science and Engineering at the University of Nagoya and the Toyota Central R&D Lab [13] is simulated by employing a typical heat pump model accordingly coupled with a kinetic model, based on the linearized Shakhov kinetic model [20,39]. The computed quantities include the operating conditions at each heat pump stage, the mass flow rate, the heat flows in the evaporator and condenser, the coefficient of performance and the overall heat pump efficiency. A detailed comparison with the corresponding experimental results is performed for five different sets of measured temperatures at the condenser, the evaporator and the inlet and outlet temperatures of the KC. Also, the effect of the geometry data, such as the length, diameter and tortuosity of the capillaries, as well as of the operating data, such as the evaporator and condenser temperatures, are investigated in detail.

The computational results are, in some cases, in reasonably good agreement with experimental data, while in other cases, significant discrepancies are observed. It has been found that the assumed material porosity and channel tortuosity are of major importance and significantly affect the KHP performance. The evaporator and condenser temperatures are also of major importance. These measured temperatures are very close to each other and therefore, very small temperature variations, even of less than 0.5%, result in significant changes in the temperature difference between the condenser and the evaporator, deducing large changes in the computed mass flow rate and heat flows. Adjustments in the assumed tortuosity and/or temperature at the heat exchangers notably improved the accuracy of model predictions, underscoring the necessity for precise characterization of the system.

Overall, the effectiveness of the employed model is well demonstrated. Furthermore, via the detailed comparison with the experimental data and the comprehensive parametric analysis, the key geometric and operational parameters affecting the performance the Knudsen compressor and the Knudsen heat pump have been identified.

Future work should prioritize refining model assumptions, increasing measurement accuracy, and exploring advanced porous structures for the Knudsen compressor. The parametric analysis demonstrated the considerable influence of geometric and operational parameters on the performance of both the KC and KHP. Optimizing these parameters, as well as relaxing some of the modeling assumptions and improving measurement accuracy will offer substantial opportunities to obtain good agreement with experiments and enhance system efficiency and performance. Such efforts are essential for the development of commercially viable KHP systems, representing a sustainable and efficient alternative to conventional micro heat pumps.

REFERENCES

[1] J.A. McLennan, Introduction to non-equilibrium statistical mechanics, Prentice-Hall, 1996.

[2] P.A. Gnoffo, Planetary-entry gas dynamics, Annual Review of Fluid Mechanics, 31, 459-494, 1999.

[3] M.S. Ivanov, S.F. Gimelshein, Computational hypersonic rarefied flows, Annual Review of Fluid Mechanics, 30, 469-505, 1998.

[4] Xudi Wang, Renchao Chang, Yunsheng Ding, Bin Zhou, Qing Cao, Hailin Bi, Characterization of the average pore diameter of nanoporous media by gas permeability measurement technique in transitional flow regime, Vacuum, Volume 194, 2021.

[5] C.M. Ho, Y.C. Tai, Micro-electro-mechanical systems (MEMS) and fluid flows, Annual Review of Fluid Mechanics, 30, 579-612, 1998.

[6] J.M. Reese, M.A. Gallis, D.A. Lockerby, New directions in fluid dynamics: non-equilibrium aerodynamic and microsystem flows, Philosophical Transactions of the Royal Society A, 361, 2967-2988, 2003.

[7] M. Knudsen, Die Molekularstroemung der Gase durch Offnungen und die Effusion, Annalen der Physik, 333(5), 999-1016, 1909.

[8] Sone, Y. (Ed.) Molecular Gas Dynamics; Birkhäuser: Boston, MA, USA, 2007.

[9] W.D. Niven, Scientific Papers of James Clerk Maxwell, Dover Publications, Inc., New York, 1965.

[10] J.H. Ferziger, H.G. Kaper, Mathematical Theory of Transport Processes in Gases, North-Holland, Amsterdam, 1972.

[11] P.L. Bhatnagar, E.P. Gross, M. Krook, A model for collision processes in gases. I. Small amplitude processes in charged and neutral one-component systems, Physical Review, 94(3), 511-525, 1953.

[12] E.M. Shakhov, Generalization of the Krook kinetic equation, Fluid Dynamics, 3(95), 1968.

[13] K. Kugimoto, Y. Hirota, T. Yamauchi, H. Yamaguchi, T. Niimi, Design and demonstration of Knudsen heat pump without moving parts free from electricity, Applied Energy, 250, 1260-1269, 2019.

[14] K. Kugimoto, Y. Hirota, T. Yamauchi, H. Yamaguchi, T. Niimi, A novel heat pump system using a multi-stage Knudsen compressor, International Journal of Heat and Mass Transfer, 127, 84-91, 2018.

[15] Qianhao Xiao, Boyan Jiang, Jun Wang, Xiaopei Yang, Dimensional analysis of hydrogen Knudsen compressor, International Journal of Hydrogen Energy, 48 (83), 32446-32458, 2023.

[16] K. Kugimoto, Y. Hirota, Y. Kizaki, H. Yamaguchi, T. Niimi, Performance prediction method for a multi-stage Knudsen pump, Physics of Fluids, 29, 12, 2017.

[17] S. Sugimoto, H. Sugimoto, Driving mechanism of thermal transpiration pump with porous material, AIP Advances, Volume 10 (10), 2020.

[18] Xiang Wang et al, A kind of refrigerant system design combined with Knudsen compressor and vortex tube, IOP Conf. Ser.: Earth Environ. Sci. 189 022064, 2018.

[19] Jianjun Ye, Xiaoyi Jiao, Shuangling Tang, Junda Shao, Zhenhua Zhao, Three dimensional channel effect on the flow characteristics and the performance of hydrogen Knudsen compressors, International Journal of Hydrogen Energy, 46 (34), 18128-18136, 2021.

[20] G. Tatsios, Internal Report, Laboratory of Physical Processes and Process Equipment, University of Thessaly, 2019.

[21] S. Nakaye, H. Sugimoto, Demonstration of a gas separator composed of Knudsen pumps, Vacuum, 125, 154-164, 2016.

[22] J. Liu, N.K. Gupta, K.D. Wise, Y.B. Gianchandani, X. Fan, Demonstration of motionless Knudsen pump based micro-gas chromatography featuring micro- fabricated columns and on-column detectors, Lab Chip, 11, 3487, 2011.

[23] Y. Qin, Y.B. Gianchandani, Flow of rarefied gas through a circular pipe, Microsyst. Nanoeng., 2, 15049, 2016.

[24] V.D. Bruggeman, Berechnung verschiedener physikalischer konstanten von heterogenen substanzen. I. dielektrizitatskonstanten und leitfahigkeiten der mischkorper aus isotropen substanzen, Ann. Phys., 416, 636-664, 1935.

[25] B. Tjaden, S.J. Cooper, D.J.L. Brett, D. Kramer, P.R. Shearing, On the origin and application of the Bruggeman correlation for analysing transport phenomena in

electrochemical systems, Current Opinion in Chemical Engineering, 12, 44-51, ISSN 2211-3398, 2016.

[26] Lihua Shen, Zhangxin Chen, Critical review of the impact of tortuosity on diffusion, Chemical Engineering Science, 62, 3748–3755, 2007.

[27] L. Pisani, Simple Expression for the Tortuosity of Porous Media. Transport in Porous Media. 88. 193-203, 2011.

[28] H.W. Piekaar, L.A. Clarenburg, Aerosol Filters- the Tortuosity Factor in Fibrous Filters. Chemical Engineering Science, 22, 1817-1827, 1967.

[29] F. Sharipov, Onsager-Casimir reciprocity relations for open gaseous systems at arbitrary rarefaction. I. General theory for single gas, Physica A, 203, 437-456, 1994.

[30] F. Sharipov, Onsager-Casimir reciprocity relations for open gaseous systems at arbitrary rarefaction. II. Application of the theory for single gas, Physica A, 203, 457-485, 1994.

[31] S.K. Loyalka, Kinetic theory of thermal transpiration and mechanocaloric effect. I, J. Chem. Phys., 55, 4497, 1971.

[32] H. Yamaguchi, P. Perrier, M. T. Ho, J. G. Méolans, T. Niimi, and I. Graur, “Mass flow measurement of thermal creep flow from transitional to slip flow regime,” Journal o Fluid Mechanics, vol. 795, pp. 690–707, 2016.

[33] O. C. Bridgeman, E. W. Aldrich, Vapor pressure tables for water, Journal of Heat Transfer, 86 (2), 279-286, 1964.

[34] Yen-Lin Han, E.P. Muntz, A. Alexeenko, M. Young, Experimental and computational studies of temperature gradient–driven molecular transport in gas flows through nano/microscale channels, Nanoscale and Microscale Thermophysical Engineering, 11 (1-2), 151-175, 2007.

[35] V. Shariati, E. Roohi, A. Ebrahimi, Numerical study of gas flow in super nanoporous materials using the direct simulation Monte-Carlo method, Micromachines,, 14, 139, 2023.

[36] F. Sharipov, Rarefied Gas Dynamics, WILEY-VCH Verlag GmbH and Co. KGaA, 2016.

[37] S. Pantazis, Simulation of transport phenomena in conditions far from thermodynamic equilibrium via kinetic theory with applications in vacuum technology and MEMS, Ph.D. Thesis, University of Thessaly, 2011.

[38] Xudi Wang, Renchao Chang, Yunsheng Ding, Bin Zhou, Qing Cao, Hailin Bi, Characterization of the average pore diameter of nanoporous media by gas permeability measurement technique in transitional flow regime, Vacuum, 194, 110596, 2021.

[39] G. Tatsios et al., Computational investigation and parametrization of the pumping effect in temperature-driven flows through long tapered channels Microfluidics and Nanofluidics, 21:99, 2017